The importance of alkyl nitrates and sea ice emissions to atmospheric NO_x sources and cycling in the summertime Southern Ocean marine boundary layer.

Jessica M. Burger[1], Julie Granger[2], Emily Joyce[3], Meredith G. Hastings[3], Kurt A.M. Spence[1], Katye E. Altieri[1]

[1]Department of Oceanography, University of Cape Town, Rondebosch, 7701, South Africa
[2]Department of Marine Sciences, University of Connecticut, Groton, 06340, USA
[3]Department of Earth, Environmental and Planetary Sciences and Institute at Brown for Environment and Society, Brown University, Providence, RI, 02906, USA.

Correspondence to: Jessica M. Burger (brgjes006@uct.ac.za)

Abstract. Atmospheric nitrate originates from the oxidation of nitrogen oxides (NO_x=NO+NO_2) and impacts both tropospheric chemistry and climate. NO_x sources, cycling, and NO_x to nitrate formation pathways are poorly constrained in remote marine regions, especially the Southern Ocean where pristine conditions serve as a useful proxy for the preindustrial atmosphere. Here, we measured the isotopic composition ($\delta^{15}N$ and $\delta^{18}O$) of atmospheric nitrate in coarse-mode (> 1μm) aerosols collected in the summertime marine boundary layer of the Atlantic Southern Ocean from 34.5°S to 70°S, and across the northern edge of the Weddell Sea. The $\delta^{15}N$-NO_3^- decreased with latitude from -2.7‰ to -42~~3~~.9~~1~~‰. The decline in $\delta^{15}N$ with latitude is attributed to changes in the dominant NO_x sources: lightning at the low latitudes, oceanic alkyl nitrates at the mid latitudes, and photolysis of nitrate in snow at the high latitudes. There is no evidence of any influence from anthropogenic NO_x sources or equilibrium isotopic fractionation. Using air mass back trajectories and an isotope mixing model, we calculate that oceanic alkyl nitrate emissions have a $\delta^{15}N$ signature of -21~~2~~.8~~0~~‰ ± 7.6~~5~~‰. Given that measurements of alkyl nitrate contributions to remote nitrogen budgets are scarce, this may be a useful tracer for detecting their contribution in other oceanic regions. The $\delta^{18}O$-NO_3^- was always less than 70‰, indicating that daytime processes involving OH are the dominant NO_x oxidation pathway during summer. Unusually low $\delta^{18}O$-NO_3^- values (less than 31‰) were observed at the western edge of the Weddell Sea. The air mass history of these samples indicates extensive interaction with sea ice covered ocean, which is known to enhance peroxy radical production. The observed low $\delta^{18}O$-NO_3^- is therefore attributed to increased exchange of NO with peroxy radicals, which have a low $\delta^{18}O$, relative to ozone, which has a high $\delta^{18}O$. This study reveals that the mid- and high-latitude surface ocean may serve as a more important NO_x source than previously thought, and that the ice-covered surface ocean impacts the reactive nitrogen budget as well as the oxidative capacity of the marine boundary layer.

1 Introduction

Atmospheric nitrate (NO_3^-), hereafter defined as gas phase nitric acid (HNO_3) and particulate NO_3^- (p-NO_3^-), impacts air quality and climate by contributing to atmospheric particulate matter (Park and Kim, 2005) ~~(Park & Kim, 2005)~~, and influencing the Earth's radiative heat budget (IPCC, 2013). It also plays a major role in the biogeochemical cycling of reactive nitrogen (Altieri et al., 2021). NO_3^- aerosols originate from the oxidation of nitrogen oxides, collectively referred to as NO_x (NO_x = NO + NO_2). NO_x cycling controls the chemical production of tropospheric ozone (O_3), a greenhouse gas and pollutant ~~(Finlayson-Pitts & Pitts, 2000)~~(Finlayson-Pitts and Pitts, 2000), which in turn contributes to the oxidising capacity of the atmosphere ~~(Alexander & Mickley, 2015)~~(Alexander and Mickley, 2015). Globally, fossil fuel combustion is the primary NO_x source ~~(van der A, et al., 2008)~~(van der A et al., 2008), which far exceeds natural emissions such as biomass burning ~~(Finlayson-Pitts & Pitts, 2000)~~(Finlayson-Pitts and Pitts, 2000), soil processes ~~(Davidson & Kingerlee, 1997)~~(Davidson and Kingerlee, 1997) and lightning ~~(Schumann & Huntrieser, 2007)~~(Schumann and Huntrieser, 2007).

Due to its remoteness, the summertime Southern Ocean (SO) marine boundary layer (MBL) can be representative of preindustrial-like atmospheric conditions ~~(Hamilton, et al., 2014)~~(Hamilton et al., 2014). The chemical composition of the Southern Ocean MBL is characterised by low NO_3^- concentrations ~~(Virkkula, et al., 2006)~~(Virkkula et al., 2006), representative of a background aerosol environment (i.e., minimal anthropogenic influence). Furthermore, the South Atlantic sector of the Southern Ocean is primarily influenced by natural NO_x sources. During summer, high lightning activity over South America and southern Africa results in NO_x production between approximately 40° S and the intertropical convergence zone (ITCZ) ~~(Nesbitt, et al., 2000)~~(Nesbitt et al., 2000). As such, lightning is expected to be the dominant NO_x source in the low latitude MBL ~~(Schumann and Huntrieser 2007, van der A, et al. 2008)~~(Schumann and Huntrieser 2007, van der A et al., 2008). Because of its pristine nature, the summertime Southern Ocean serves as a unique region in which to study atmospheric chemistry and is a useful preindustrial reference point for comparing the magnitude of anthropogenic aerosol impacts on climate ~~(Haywood and Boucher 2000, Hamilton, et al. 2014)~~(Haywood and Boucher 2000; Hamilton et al., 2014).

The atmospheric chemistry of the polar MBL at the high southern latitudes differs from that of the mid- and low-latitude MBL. During summer, high levels of photochemistry result in the emission of reactive gases from sea ice and snow cover in the Antarctic. As a result, highly elevated concentrations of hydrogen oxide radicals (HO_x = OH + peroxy radicals), halogens, nitrous acid (HONO), and NO_x have been observed during spring and summer in the polar regions (Brough et al., 2019). Furthermore, photochemical production of NO_x within the surface snow of Antarctica and subsequent oxidation in the overlying atmosphere represents a significant NO_3^- source to the Antarctic troposphere (Jones et al., 2000, 2001)~~(Jones, et al., 2000; Jones, et al., 2001)~~. NO_3^- photolysis near the surface-air interface of ice crystals produces NO_2 ~~(Grannas, et al. 2007, Jones, Weller and Wolff, et al. 2000)~~(Grannas et al. 2007; Jones et al., 2000), which can be released to the firn (i.e., the intermediate stage of ice between snow and glacial ice) air and escape the snowpack to the overlying atmosphere (Erbland~~,~~ et al., 2013; Shi~~,~~ et al., 2015; Shi~~,~~ et al., 2018). During winter, additional NO_x sources to the Antarctic atmosphere may include

long-range transported peroxyacetyl nitrates (PAN) and stratospheric inputs (Savarino~~,~~ et al., 2007; Lee~~,~~ et al., 2014; Walters~~,~~ et al., 2019).

Emission of alkyl nitrates (a group of nitrogen gases collectively referred to as $RONO_2$) from the surface ocean have been recently proposed as a potential NO_x source to the MBL in remote regions (Williams~~,~~ et al., 2014; Fisher et al., 2018). Observations of elevated MBL alkyl nitrate concentrations suggest that a direct oceanic source exists in both the tropics ~~(Atlas, et al., 1993; Blake, et al., 2003)~~(Atlas et al., 1993; Blake et al., 2003), and the high-latitude Southern Ocean ~~(Blake, et al., 1999; Jones, et al., 1999)~~(Blake et al., 1999; Jones et al., 1999). Although the exact mechanism remains unclear, experimental evidence suggests that oceanic $RONO_2$ production occurs via photochemical processes involving the aqueous phase reaction of RO_2, derived from the photolysis of oceanic dissolved organic matter and NO, derived from seawater nitrite photolysis ~~(Dahl, et al., 2003; Dahl & Saltzman, 2008)~~(Dahl et al., 2003; Dahl and Saltzman, 2008). Supersaturated $RONO_2$ conditions in the surface ultimately drive a net flux from the ocean to the atmosphere ~~(Chuck, et al., 2002; Dahl, et al., 2005)~~(Chuck et al., 2002; Dahl et al., 2005). The photolysis of emitted $RONO_2$ and subsequent OH oxidation in the overlying atmosphere leads to NO_x formation ~~(Fisher, et al., 2018)~~ (Fisher et al., 2018), and /or~~,~~ $RONO_2$ can form aerosol NO_3^- directly by hydrolysis (Rindelaub et al., 2015).

Current global atmospheric models suggest that oceanic $RONO_2$ represents a significant source of nitrogen (N) to the Southern Ocean MBL, accounting for 20% to 60% of the reactive N pool at the high-latitudes (60° S to 90° S) ~~(Fisher, et al., 2018)~~(Fisher et al., 2018). However, only one ~~small~~ shipborne dataset with coincident ocean-atmosphere $RONO_2$ concentration measurements exists to substantiate this notion (Hughes et al., 2008). Additionally, the NO_x source from $RONO_2$ degradation dominates relative to model defined primary NO_x emission sources over the SO, which include shipping, aircraft and lightning ~~(Fisher, et al., 2018)~~(Fisher et al., 2018). However, the lack of seawater observations available to constrain Southern Ocean $RONO_2$ distributions hamper the validation of model fluxes. Better understanding of the Southern Ocean $RONO_2$ source is required to improve simulations and accurately evaluate its contribution to the Southern Ocean MBL NO_x budget.

1.1 Natural abundance isotopes of atmospheric nitrate

Measurements of the oxygen (O) and N stable isotope ratios of atmospheric NO_3^- can be used to constrain NO_x sources, NO-NO_2 cycling, and NO_x to NO_3^- oxidation pathways, which are critical for~~to our~~ understanding ~~of~~ the reactive N budget in the atmosphere. This technique has been applied in ~~both~~ polluted ~~(Elliot, et al., 2007; Zong, et al., 2017)~~(Elliot et al., 2007; Zong et al., 2017), open ocean ~~(Hastings, et al., 2003; Morin, et al., 2009; Kamezaki, et al., 2019; Gobel, et al., 2013; Altieri, et al., 2013)~~(Hastings et al., 2003; Morin et al., 2009; Kamezaki et al., 2019; Gobel et al., 2013; Altieri et al., 2013), and polar environments (Morin et al., 2009; Walters et al., 2019). Stable isotope ratios are reported as a ratio of the heavy to light isotopologues of a sample relative to the constant isotopic ratio of a reference standard, using delta (δ) notation in units of "per mil" (‰) following Eq. (1):

$$\delta = \left(\left(R_{sample}/R_{standard}\right) - 1\right) \times 1000 \quad (1)$$

where *R* represents the ratio of $^{15}N/^{14}N$ or $^{18}O/^{16}O$ in the sample and in the reference standard, respectively. The reference for O is Vienna Standard Mean Ocean Water (VSMOW) and for N is atmospheric N_2 ~~(Bolhke, et al., 2003)~~(Bölhke et al., 2003).

When NO_x is converted to NO_3^-, the N atom is conserved. As such, it is generally expected that the N stable isotope ratio of atmospheric NO_3^- ($\delta^{15}N\text{-}NO_3^-$) reflects the $\delta^{15}N$ of the source NO_x, ~~(Kendall, et al., 2007)~~(Kendall et al., 2007) plus any isotopic fractionation associated with NO/NO_2 cycling or NO_x to NO_3^- conversion. For example, the $\delta^{15}N$ of lightning generated NO_x is close to 0‰ (Hoering, 1957) and is distinct from stratospheric and snowpack NO_x. Savarino et al., (2007) used the degree of N_2O destruction in the stratosphere and the associated isotopic fractionation to derive an Antarctic stratospheric $\delta^{15}N\text{-}NO_x$ source signature of 19‰ ± 3‰ ~~(Savarino, et al., 2007)~~(Savarino et al., 2007). In contrast, snow emitted NO_x typically has a very low $\delta^{15}N$ signature due to the large fractionation ($^{15}\varepsilon$~~ϵ~~) of ~ - 48‰ (Berhanu et al., 2014, ~~and~~ 2015) associated with NO_3^- photolysis in the snowpack, where $^{15}\varepsilon$~~ϵ~~ = (KIE -1) x 1000‰ and the kinetic isotope effect (KIE)~~of a reaction~~ is the ratio of the rates with which the two isotopes of N are converted from reactant to product. If equilibrium isotope fractionation during NO/NO_2 cycling occurs, it results in the ^{15}N enrichment of NO_2 such that the NO_3^- formed from this NO_2 will have a higher $\delta^{15}N\text{-}NO_3^-$ than the initial NO_x source ~~(Freyer, et al., 1993; Walters, et al., 2016)~~(Freyer et al., 1993; Walters et al., 2016). Equilibrium isotope fractionation during the transformation of NO_x to NO_3^- also results in higher $\delta^{15}N\text{-}NO_3^-$ compared to the original NO_x source ~~(Walters & Michalski, 2015)~~(Walters and Michalski, 2015).

In contrast to N, the O stable isotope ratio of atmospheric NO_3^- ($\delta^{18}O\text{-}NO_3^-$) is reflective of the oxidants involved in NO_x cycling prior to NO_3^- formation, as well as the dominant NO_3^- formation pathway (Hastings~~,~~ et al., 2003; Michalski~~,~~ et al., 2003; Alexander~~,~~ et al., 2020). The O atoms of NO_x are rapidly exchanged with oxidising agents in the atmosphere to produce NO_3^-. Tropospheric NO_x recycles rapidly with O_3 following the equations below:

$$NO + O_3 \rightarrow NO_2 + O_2 \quad \text{(R1)}$$

$$NO_2 + O_2 + h\nu \rightarrow NO + O_3 \quad \text{(R2)}$$

The oxidation of NO to NO_2 requires an atmospheric oxidant, typically O_3 throughout most of the troposphere (R1), while the breakdown of NO_2 back to NO is photolytic and requires light (R2). Therefore, under nighttime/dark conditions (R2) shuts down and NO_x is comprised almost entirely of NO_2.

The dominant daytime sink for NO_x is the oxidation of NO_2 by OH, which produces nitric acid (HNO_3) via (R3), where M is a non-reacting molecule.

$$NO_2 + OH + M \rightarrow HNO_3 + M \quad \text{(R3)}$$

Under nighttime/dark conditions, the photolytic production of OH cannot occur and NO_2 is oxidised by O_3 (R4). HNO_3 is ultimately formed via the hydrolysis of dinitrogen pentoxide (N_2O_5), following the reactions (R5) and (R6) below:

$$NO_2 + O_3 \rightarrow NO_3 + O_2 \quad \text{(R4)}$$

$$NO_3 + NO_2 + M \rightleftharpoons N_2O_5\,(g) + M \quad \text{(R5)}$$

$$N_2O_5\,(g) + H_2O\,(l) + \text{surface} \rightarrow 2HNO_3\,(aq) \quad \text{(R6)}$$

NO_3 can also react with hydrocarbons (HC) (e.g., dimethylsulphide (DMS)) to form HNO_3 following reaction (R7) below:

NO_3 + HC/DMS → HNO_3 + products (R7)

Lastly, in regions with elevated halogen concentrations, NO_2 can be oxidised by reactive halogens, for example bromine oxide (BrO), to form HNO_3 following (R8) and (R9) below:

NO_2 + BrO → $BrONO_2$ (R8)

$BrONO_2$ + H_2O + surface → HNO_3 + HOBr (R9)

Typically, aerosol $\delta^{18}O\text{-}NO_3^-$ is interpreted as being determined by the dominant NO_x oxidation pathways, (R3) versus (R4) to (R9). If some combination of R4-R9 occurs, then O_3 is the main oxidant, whereas during (R3), one of the O atoms originates from OH. The OH radical exchanges with H_2O vapor in the troposphere, therefore the $\delta^{18}O$ of OH is a function of the $\delta^{18}O$ of H_2O vapour, which generally ranges from -27.5‰ to 0‰ in the subtropics and over the Southern Ocean ~~(Michalski, et al., 2012; Guilpart, et al., 2017; Dar, et al., 2020)~~(Michalski et al., 2012; Guilpart et al., 2017; Dar et al., 2020), and equilibrium isotope exchange between OH and H_2O ~~(Walters & Michalski, 2016)~~(Walters and Michalski, 2016). In contrast the $\delta^{18}O$ of tropospheric O_3 is much higher, the most recent estimate being 114.8±10.4‰ ~~(Vicars & Savarino, 2014)~~(Vicars and Savarino, 2014). Therefore, a higher $\delta^{18}O$ for atmospheric NO_3^- reflects the increased influence of O_3 on NO_x to NO_3^- conversion (R4-R9), and the $\delta^{18}O\text{-}NO_3^-$ is lower when (R3) is favoured, due to the lack of exchange of O atoms with O_3 ~~(Hastings, et al., 2003; Fang, et al., 2011; Altieri, et al., 2013)~~(Hastings et al., 2003; Fang et al., 2011; Altieri et al., 2013).

Here, we present the concentration and isotopic composition of coarse mode (> 1 μm) atmospheric NO_3^- collected in the MBL of the Southern Ocean between Cape Town, South Africa and coastal Antarctica, as well as across the Weddell Sea gyre, during summer. Using air mass back trajectories, surface ocean nitrite measurements, and the aerosol $\delta^{15}N$- and $\delta^{18}O\text{-}NO_3^-$, we address 1) the major NO_x sources as well as the main oxidants in NO/NO_2 cycling and NO_x to NO_3^- conversion across a large latitudinal transect of the Atlantic Southern Ocean and within the Weddell Sea gyre, and 2) the influence of sea-ice and snowpack emissions on NO_x/NO_3^- chemistry in the high-latitude MBL.

2) Methods

2.1) Sample collection

Samples were collected on board the Research Vessel (R/V) *SA Agulhas II* during one cruise subdivided into three legs. Leg one refers to the voyage south from Cape Town (33.9° S, 18.4° E) to Penguin Bukta (71.4° S, 2.5° W) in early summer (7 ~~December 2018~~ to 19 December 2018) as part of the South African National Antarctic Expedition's annual relief voyage (SANAE 58). Leg two is the Weddell Sea Expedition (WSE) from 4 January ~~2019~~ to 21 February 2019. All data were recorded in GMT. The WSE refers to the voyage west from Penguin Bukta to the northern edge of the Weddell Sea gyre to Larsen C ice shelf, followed by a detour to King George Island before returning to the Weddell Sea and sailing back to Penguin Bukta. Leg three refers to the SANAE 58 return voyage north from Penguin Bukta to Cape Town in late summer (27 February ~~2019~~ to 15 March 2019). From here on, legs one, two and three will be referred to as early summer, the Weddell Sea, and late summer, respectively.

Size-segregated atmospheric aerosols were collected on the ninth floor above the bridge (approximately 20 m above sea level), using a high-volume air sampler (HV-AS; Tisch Environmental). Air was pumped at an average flow rate of 0.82 m^3 min^{-1} though a five-stage cascade impactor (TE-235; Tisch Environmental), loaded with combusted (400°C for 4 hours) glass fibre filters (TE-230-GF; Tisch Environmental) that have a surface area of approximately 119 cm^2. Aerosol nitrate in the MBL is predominantly present in the coarse mode (> 1 µm), therefore only filter stages 1 through 4 were analysed, where the aerodynamical diameter of particles collected are as follows: stage 1 (> 7 µm); stage 2 (3 to 7 µm); stage 3 (1.5 to 3 µm) and stage 4 (1 to 1.5 µm).

A sector collector was used to restrict HV-AS activity to avoid contamination from ship stack emissions (Campbell Scientific Africa). The HV-AS only began operating if the wind was blowing at an angle less than 75° or greater than 180° from the bow of the ship for a minimum of ten minutes at a speed of at least 1 m s^{-1}. Filters were removed from the cascade impactor inside a laminar flow cabinet (Air Science), placed in individual zip-sealed plastic bags and stored at -20°C until analysis.

Given that the MBL of the Southern Ocean is characterised by low atmospheric NO_3^- concentrations, an attempt was made to ensure that at least 24 hours of in-sector sampling had passed before filters were removed from the cascade impactor. However, this was not always possible as on occasion the filters had to be removed early to avoid contamination due to unusual ship manoeuvres or~~resulting in~~ stagnant conditions. Therefore, sampling times ranged between 13 and 88 hours across the three legs. The details of each cruise leg can be found in the supplemental information (Table S1).

During the research voyage, a field blank was collected by fitting the cascade impactor with a set of filters and walking the cascade impactor from the laboratory to the HV-AS in the same way that atmospheric samples were deployed. The cascade impactor was placed into the HV-AS and then immediately removed without the HV-AS turning on, after which the filters were removed from the cascade impactor and stored in the same manner as the atmospheric samples. All chemical analyses performed on samples were also performed on the field blank~~s~~ filters to assess possible contamination during filter deployment or sample handling.

2.2) Sample analysis

Filter stages 1 to 4 were extracted using ultra-clean deionised water (DI; 18.2 MΩ) under a laminar flow cabinet (Air Science). The extraction ratio was approximately 30 cm^2 of filter in 25 mL of DI. Extracts were immediately sonicated for one hour and then stored at 4°C for at least 12 hours. Thereafter, extracts were filtered (0.2 µm) using an acid washed syringe into a clean 30 mL HDPE bottle and stored at -20°C until analysis (Baker~~,~~ et al., 2010).

Aerosol nitrate concentrations ($[NO_3^-]$) were determined using a Thermo Scientific Dionex Aquion Ion Chromatography (IC) system ~~equipped with an autosampler~~ (precision of ± 0.3 µmol L^{-1}). The anion IC contained an AG22 RFIC 4 x 50 mm guard column and AG22 RFIC 4 x 250 mm analytical column. A six-point standard curve that encompassed the range of sample concentrations (extract $[NO_3^-]$: 1.3 to 27.7 µmol L^{-1}) was run on each day of analysis (Dionex Seven Anion-II Standard) and an R^2 value > 0.999 was required for sample analysis to proceed. Final aerosol $[NO_3^-]$ were corrected by subtracting the

field blanks, which- represented 35% of the total [NO_3^-] on average. had an average of 484.7 nmol NO_3^- per filter deployment. The pooled standard deviation (Sp) of four repeated sample measurements for [NO_3^-] was 0.3 µmol L^{-1}. A subset ofA aerosol samples were additionallyalsoas analysed for [NO_3^-] using a Lachat QuikChem® flow injection autoanalyzer (precision of ± 0.8 µmol L^{-1}). TFor the subset of samples analysed using both instruments, the average [NO_3^-] measured using the Lachat QuikChem® flow injection autoanalyzer and the IC system is reported (Table S3).

Nitrogen and oxygen isotopic ratios were measured using the denitrifier method (Sigman, et al., 2001 and Casciotti, et al., 2002). To determine the $^{15}N/^{14}N$ and $^{18}O/^{16}O$ of NO_3^-, a natural strain of denitrifying bacteria, *Pseudomonas aureofaciens*, that lack the terminal nitrous oxide (N_2O) reductase enzyme were used to convert aqueous NO_3^- quantitatively to N_2O gas. The product N_2O was analysed by continuous flow isotope ratio mass spectrometry (IRMS) using a Delta V Advantage IRMS interfaced with an online N_2O extraction and purification system. Individual analyses were referenced to injections of N_2O from a pure gas cylinder and then standardized through comparison to the international reference materials of IAEA-N3 and USGS34 for $\delta^{15}N\text{-}NO_3^-$, and IAEA-N3, USGS34 and USGS35 for $\delta^{18}O\text{-}NO_3^-$ (Table S2) (Böhlke et al., 2003). The $^{15}N/^{14}N$ of samples was corrected for the contribution of ^{17}O to the peak at mass 45 using an average reported $\Delta^{17}O$ value of 26‰ from atmospheric nitrate collected in the Weddell Sea (Morin, et al., 2009)(Morin et al., 2009). The pooled standard deviation for all measurements of IAEA-N3 and USGS34 for $\delta^{15}N\text{-}NO_3^-$, and IAEA-N3, USGS34 and USGS35 for $\delta^{18}O\text{-}NO_3^-$ are reported (Table S2). All samples were measured in triplicate in separate batch analyses. The pooled standard deviation from all replicate analyses of samples was 0.25‰ for $\delta^{15}N\text{-}NO_3^-$ and 0.64‰ for $\delta^{18}O\text{-}NO_3^-$. The average $\delta^{15}N\text{-}NO_3^-$ and $\delta^{18}O\text{-}NO_3^-$ computed for each filter deployment was weighted by the [NO_3^-] observed for each stage and error was propagated according to standard statistical practises (Table S3).

Seawater samples were collected in triplicate every two hours from the ship's underway system (position at depth approximately± 5 m) for the analysis of surface ocean nitrite concentrations ([NO_2^-]). [NO_2^-] was analysed using the colorimetric method of Grasshof et al. (1983) using a Thermo Scientific Genesys 30 visible spectrophotometer (detection limit of 0.05 µmol L^{-1}) (Table S4). .

2.36) Air mass back trajectory analysis

To determine the air mass source region for each aerosol sample, air mass back trajectories (AMBTs) were computed for each hour in which the HV-AS was operational for at least 45 minutes of that hour. Given that the ship was moving, a different date, time and starting location was used to compute each AMBT. An altitude of 20 m was chosen to match the height of the HV-AS above sea level and 72-hour AMBTs were computed to account for the lifetime of NO_3^- in the atmosphere. All AMBTs were computed with NOAA's Hybrid Single-Particle Lagrangian Integrated Trajectory model (HYSPLIT v 4), using NCEP Global Data Assimilation System (GDAS) output, which can be accessed at https://www.arl.noaa.gov/ready/hysplit4.html (NOAA Air Resources Laboratory, Silver Spring, Maryland) (Stein, et al., 2015; Rolph, 2016).

3) Results

The coarse mode (> 1 μm in diameter) aerosol [NO_3^-] computed by summing the [NO_3^-] of stages 1 through 4, ranged from 15.1~~22.3~~ to 235.0~~374.2~~ ng m^{-3} (Fig. 1a~~A~~ and Table 1). The mass-weighted $\delta^{15}N$ of coarse mode aerosol NO_3^- ranged from -43.1‰ to -2.7‰ (Figs. 1b~~B~~, 2 and Table 1). There were no clear trends in atmospheric [NO_3^-] or $\delta^{15}N$-NO_3^- with aerosol size (Table S5).

The highest nitrate concentrations occurred between 34° S and 45° S, and then decreased with increasing latitude. Similarly, higher values characterized $\delta^{15}N$-NO_3^- between 34° S and 45° S (-4.9 ± 1.3‰), and then decreased with increasing latitude (Fig. S2). At the high ~~-~~latitudes (south of 60° S), median values of 26~~41~~.21~~7~~ ng m^{-3} and -22.2‰ were observed for nitrate concentration and $\delta^{15}N$, respectively. Coincident mass-weighted $\delta^{18}O$-NO_3^- values ranged from 16.5‰ to 70‰ (Figs. 1c~~C~~, 3 and Table 1). No latitudinal trend in $\delta^{18}O$-NO_3^- was apparent, although distinctly low $\delta^{18}O$-NO_3^- values were observed in the Weddell Sea, as discussed in section 4.3 below. The difference between $\delta^{18}O$-NO_3^- observed in the Weddell Sea (during January to February) and $\delta^{18}O$-NO_3^- observed at corresponding latitudes (56° S to 70° S) during the early and late summer transects is statistically significant (p-value ~~=<~~ 0.00~~95~~). The early and late summer cruise transects were similar spatially in that both took place along the same hydrographic line (i.e., the Good Hope line), apart from the deviation to South Georgia during late summer (Fig. 2a~~A~~ & b~~B~~). Even though the early and late summer cruise transects occurred in December and March, respectively, there is no statistically significant difference in [NO_3^-] (p-value = 0.43), $\delta^{15}N$-NO_3^- (p-value = 0.53) or $\delta^{18}O$-NO_3^- (p-value = 0.67) between them ~~(p-value > 0.05 in all cases)~~. Therefore, the early and late summer legs are discussed together and collectively referred to as the latitudinal transect.

Table 1: The average (Avg), standard deviation (SD) and range of total coarse-mode (> 1μm) atmospheric nitrate concentration ([NO_3^-]; ng m^{-3}) and the mass weighted average N and O isotopic composition of coarse mode nitrate ($\delta^{15}N$-NO_3^- and $\delta^{18}O$-NO_3^-; ‰) are shown. Cruise legs are denoted as follows: early summer (ES), Weddell Sea (WS) and late summer (LS).

Leg	[NO_3^-] (ng m^{-3})		$\delta^{15}N$-NO_3^- (‰ vs. N_2)		$\delta^{18}O$-NO_3^- (‰ vs. VSMOW)	
	Avg (SD)	Range	Avg (SD)	Range	Avg (SD)	Range
ES	88.1~~139~~ (70.2~~112.8~~)	20.0~~31.9~~ to 235.0~~374.2~~	-19.5 (16.4)	-42.9 to -2.7	47.1 (17.8)	16.5 to 70.0
WS	29.4~~46.7~~ (12.1~~19.5~~)	15.1~~22.3~~ to 59.5~~94.8~~	-22.7 (7.2)	-38.1 to -11.6	38.4 (12.9)	18.8 to 60.3
LS	59.7~~94.0~~ (59.4~~95.5~~)	16.9~~22.3~~ to 177.4~~282.5~~	-15.0 (8.1)	-25.6 to -4.6	50.3 (6.3)	43.1 to 58.9

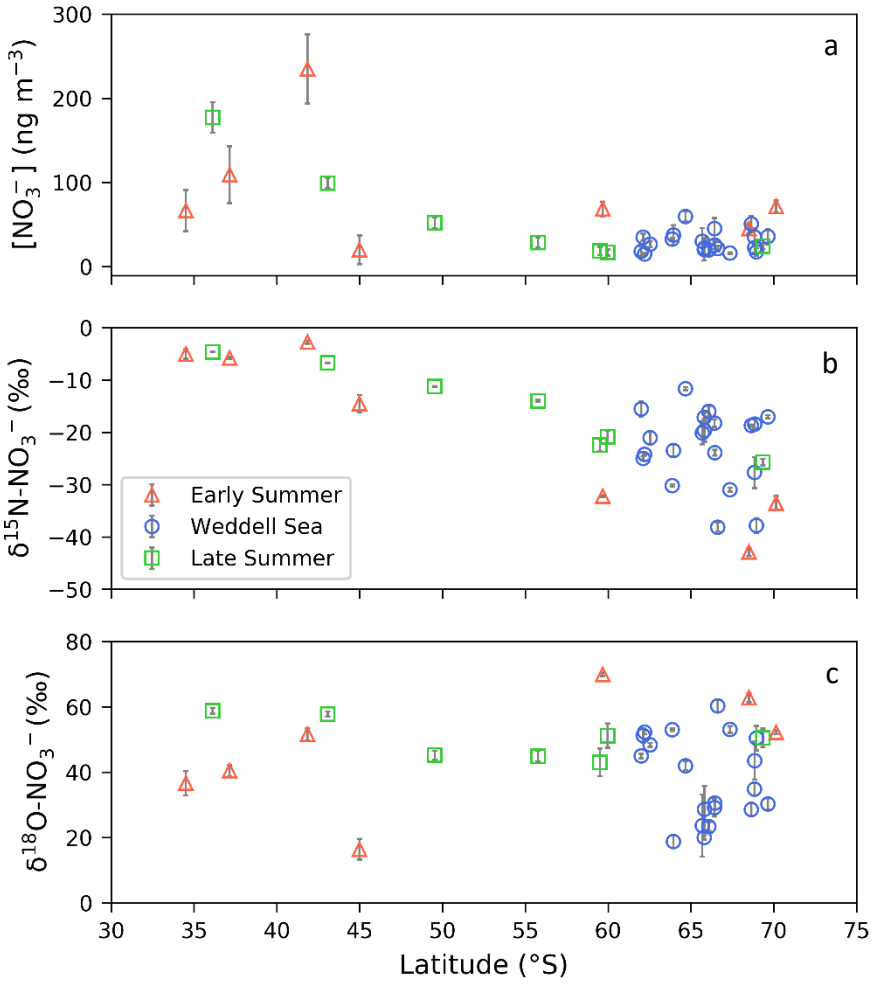

Figure. 1. (a) The average (± 1 SD) coarse mode (> 1 µm) nitrate concentration [NO_3^-] (ng m^{-3}; a), and the weighted average (± 1 SD) $\delta^{15}N$ (b) and $\delta^{18}O$ (c) of atmospheric nitrate ($\delta^{15}N\text{-}NO_3^-$ (‰ vs. N_2) and $\delta^{18}O\text{-}NO_3^-$ (‰ vs. V-SMOW), respectively), as a function of latitude (°S). Early and late summer latitudinal transects are denoted by the red triangles and green squares, respectively. Weddell Sea samples are denoted by blue circles. Where error bars (± 1 SD) are not visible, the standard deviation is smaller than the size of the marker.

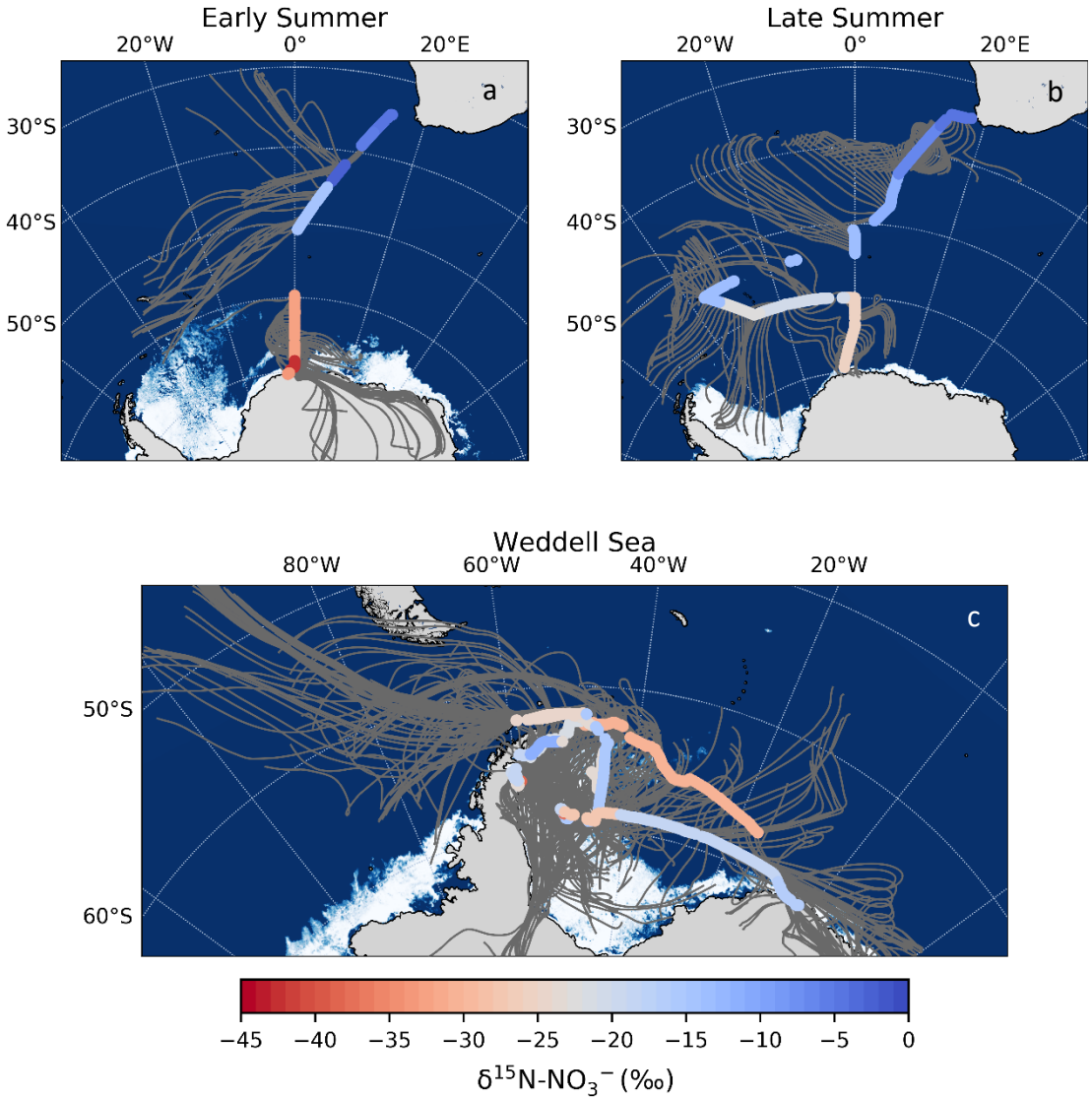

Figure 2. 72-hour AMBTs (grey lines) computed for each hour of the voyage when the HV-AS was operational for more than 45 minutes of the hour during early summer (a), late summer (b), and in the Weddell Sea (c). The colour bar represents the weighted average $\delta^{15}N$ of coarse mode (> 1 µm) atmospheric nitrate ($\delta^{15}N\text{-}NO_3^-$). Individual AMBTs for each aerosol sample from the Weddell Sea are shown in Fig. S1. The white represents the location of the sea ice determined using satellite derived sea-ice concentration data, obtained from passive microwave sensors AMSR2 (Advanced Microwave Scanning Radiometer 2, Spreen et al., 2008).

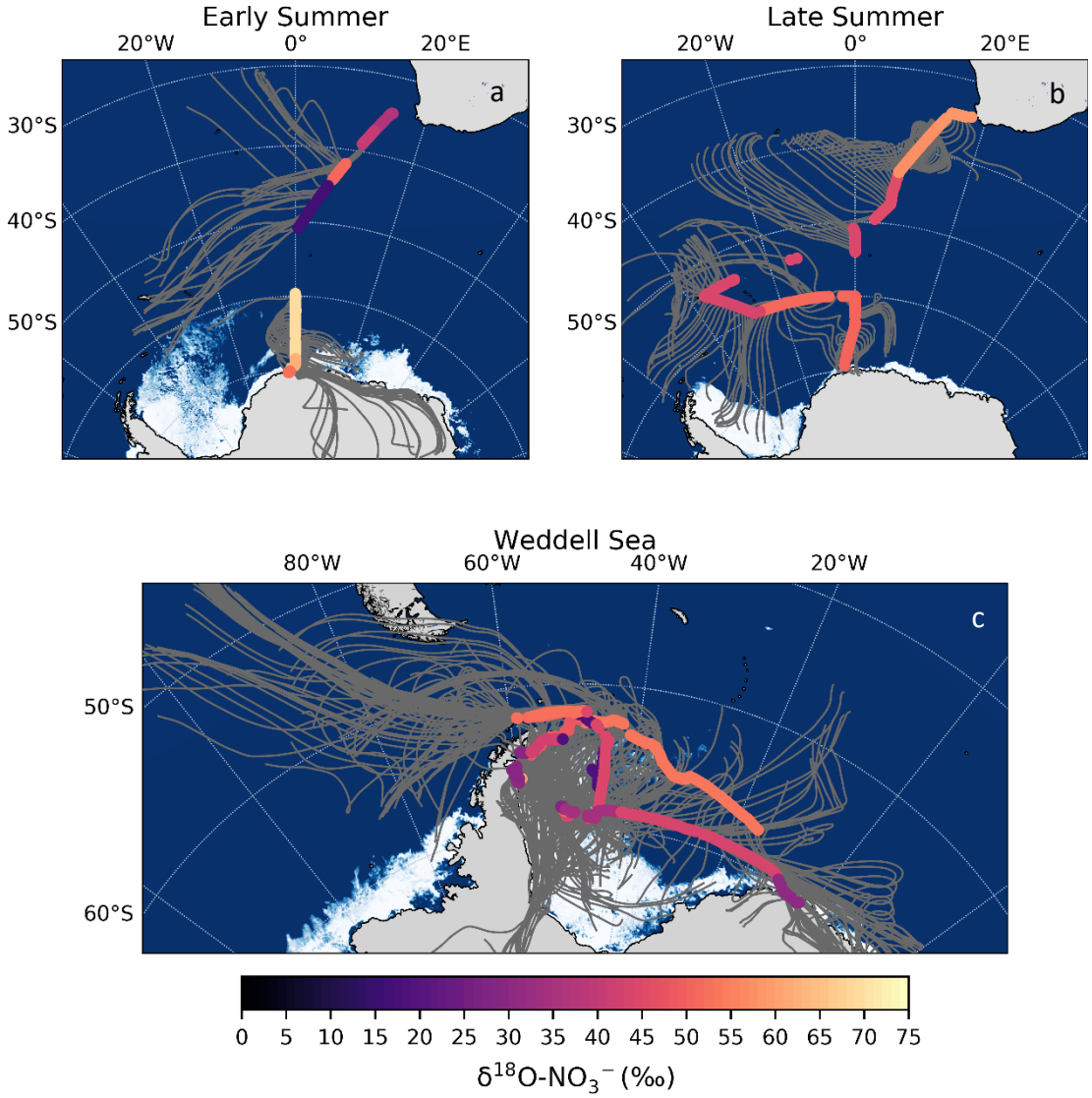

Figure. 3. 72-hour AMBTs (grey lines) computed for each hour of the voyage when the HV-AS was operational for more than 45 minutes of the hour during early summer (aA), late summer (bB), and in the Weddell Sea (cC). The colour bar represents the weighted average $\delta^{18}O$ of coarse mode (> 1 µm) atmospheric nitrate ($\delta^{18}O$-NO_3^-). Individual AMBTs for each aerosol sample from the Weddell Sea are shown in Fig. S1 The white represents the location of the sea ice (see Fig. 2 caption).

4) Discussion

OThe sum of our observations reveals a latitudinal gradient in atmospheric NO_3^- concentration and $\delta^{15}N$-NO_3^-, which we hypothesize may be attributed to the varying contribution of the dominant NO_x sources present between Cape Town and coastal

Antarctica. In contrast, $\delta^{18}O\text{-}NO_3^-$ depicts no latitudinal trend~~;~~, however,~~ very~~ relatively low $\delta^{18}O\text{-}NO_3^-$ values are observed in the Weddell Sea, which we hypothesize may be attributed to the influence of sea ice emissions on NO_x cycling. Below, we first discuss the extent to which anthropogenic NO_x sources may influence the observed atmospheric NO_3^- concentrations and $\delta^{15}N$ signatures. Then we discuss the dominant NO_x sources to low, mid and high latitude Southern Ocean MBL NO_3^-, determined in part from 72-hour AMBT~~'~~s, as well as the role of various oxidants in NO/NO_2 cycling and NO_2 oxidation.

4.1) Minimal influence of anthropogenic NO_x sources

Aerosol NO_3^- concentrations were low (< 100 ng m^{-3}; Fig. 1a~~A~~) for most air masses sampled along the latitudinal transect and in the Weddell Sea, consistent with the expectation of minimal influence from anthropogenic NO_x sources. For comparison, [NO_3^-] in a polluted urban airshed over South Africa can be > 500 ng m^{-3} (Collett et al., 2010). Interestingly, NO_3^- concentrations were higher (± 2~~3~~00 ng m^{-3}; Fig. 1a~~A~~) in samples collected near the South African coast at the beginning of the latitudinal transect (i.e., above 43° S). However, 72-hour AMBTs computed for all latitudinal transect samples indicate that sampled air masses originated from over the South Atlantic sector of the Southern Ocean (Fig. 2a~~A~~ and 2b~~B~~), with no continental influence and limited opportunity for direct anthropogenic NO_x emissions to contribute to aerosol NO_3^-, assuming NO_3^- has a lifetime of 72 hours (Alexander~~,~~ et al., 2020). Furthermore, contamination from ship stack emissions was avoided by using a sector collector to restrict HV-AS activity to certain wind directions (Sect. 2.1). As such, the higher atmospheric NO_3^- concentrations observed near South Africa are best explained by greater lightning NO_x production, which generally occurs between 40° S and the ITCZ during summer ~~(Nesbitt, et al., 2000; van der A, et al., 2008)~~(Nesbitt et al., 2000; van der A et al., 2008).

4.2) Interpretation of natural NO_x sources using the N isotopic composition of atmospheric NO_3^-

Aerosol $\delta^{15}N\text{-}NO_3^-$ ranged from -2.7‰ for low-latitude air masses to -42.9‰ for high-latitude air masses (including those sampled in the Weddell Sea; Fig. 1b~~B~~). As discussed in section 1.1, the $\delta^{15}N\text{-}NO_3^-$ reflects the $\delta^{15}N$ of the source NO_x plus any isotopic fractionation imparted from NO/NO_2 cycling or NO_x to NO_3^- conversion. Similar to previous studies, we surmise that NO_x equilibrium fractionation is unlikely to be relevant in our system, as NO_x concentrations are significantly lower than O_3 concentrations (Elliott~~,~~ et al., 2007; Morin~~,~~ et al., 2009; Walters~~,~~ et al., 2016; Park~~,~~ et al., 2018). Typical O_3 concentrations observed at coastal sites in Antarctica are on the order of 20 ppbv (parts per billion by volume) ~~(Nadzir, et al., 2018)~~(Nadzir et al., 2018), whereas the sum of NO and NO_2 rarely exceeds 0.0~~4~~40 ppb~~t~~v ~~(Jones, et al., 2000; Weller, et al., 2002; Bauguitte, et al., 2012)~~(Jones et al., 2000; Weller et al., 2002; Bauguitte et al., 2012). Under these conditions NO_x isotopic exchange occurs at a much slower rate than (R1) and (R2), such that little to no equilibrium isotope fractionation is expressed and the $\delta^{15}N$ of the NO_3^- should reflect the $\delta^{15}N$ of the NO_x source ~~(Walters, et al., 2016)~~(Walters et al., 2016). Additionally, equilibrium isotope effects are temperature dependent (increasing with decreasing temperature) and here ambient temperatures decline with increasing latitude. Therefore, if equilibrium isotope fractionation were occurring during $NO\text{-}NO_2$ cycling and/or

NO_x to NO_3^- conversion, one would expect $\delta^{15}N\text{-}NO_3^-$ to increase with latitude, as both fractionation processes produce NO_3^- with a $\delta^{15}N$ signature higher than the source NO_x. However, the opposite trend is observed here whereby $\delta^{15}N\text{-}NO_3^-$ decreases with increasing latitude (Fig. 1b~~B~~). Therefore, we discount the hypothesis that equilibrium isotope effects can explain the latitudinal gradient in $\delta^{15}N\text{-}NO_3^-$.

NO_3^- in the Antarctic troposphere may also derive from stratospheric denitrification, whereby HNO_3 is injected into the troposphere from the stratosphere via the subsidence and penetration of polar stratospheric clouds (PSC). However, this phenomenon typically occurs in winter when the tropospheric barrier is weak and the lower stratosphere is cold enough for PSC formation ~~(Savarino, et al., 2007; Walters, et al., 2019)~~(Savarino et al., 2007; Walters et al., 2019). Furthermore, $\delta^{15}N\text{-}NO_3^-$ originating from stratospheric inputs is estimated to be 19‰ ± 3‰ ~~(Savarino, et al., 2007)~~(Savarino et al., 2007), a value substantially greater than the atmospheric $\delta^{15}N\text{-}NO_3^-$ observed here for high-latitude air masses; thus, we discount a direct influence from stratospheric NO_x. We propose that the observed variation in atmospheric $\delta^{15}N\text{-}NO_3^-$ across the Southern Ocean is ~~therefore~~ best explained by the changing contribution of three dominant NO_x sources: lightning, surface ocean alkyl nitrate emissions, and photochemical production on snow and ice, determined using AMBT analyses and typical NO_x source signatures where possible, as discussed below.

4.2.1) High-latitudes: Photochemical NO_x source

Aerosol $\delta^{15}N\text{-}NO_3^-$ was relatively~~very~~ low in air masses from the southern high-latitudes, including in the Weddell Sea (average of -24.3‰; Figs. 1b~~B~~ & 2). The latitudinal gradient in lightning NO_x production suggests that lightning NO_x is greatly reduced ~~production via this mechanism is greatly reduced~~ at high ~~-~~latitudes ~~(Nesbitt et al., 2000)~~(Savarino, et al., 2007). Similar to other studies in the region ~~(Savarino, et al., 2007; Morin, et al., 2009)~~(Savarino et al., 2007; Morin et al., 2009), we suggest that photochemical NO_x production on snow or ice accounts for the low aerosol $\delta^{15}N\text{-}NO_3^-$ in high-latitude air masses, where high-latitude air mass samples are defined as those exposed to the Antarctic continent or the surrounding sea ice (with sea ice concentration being at least 50%) ~~(Fig. 4, red)~~. Antarctic estimates for isotopic fractionation associated with snow NO_3^- photolysis during summer range from -47.9‰ to -55.8‰ for laboratory and field experiments, respectively (Berhanu~~,~~ et al., 2014, 2015), resulting in the emission of low $\delta^{15}N$ NO_x to the overlying atmosphere ~~(Savarino, et al., 2007; Morin, et al., 2009; Shi, et al., 2018; Walters, et al., 2019)~~(Savarino et al., 2007; Morin et al., 2009; Shi et al., 2018; Walters et al., 2019). Therefore, NO_3^- photolysis explains the very low $\delta^{15}N\text{-}NO_3^-$ observed in high-latitude air masses in early and late summer that crossed snow-covered continental ice or sea ice before being sampled (Figs. 2a & b ~~and 4~~). During early summer, air masses spent significantly more time over the snow-covered continent compared to late summer ~~(Figs. 2A & B)~~ and the sea ice extent was greater in early summer compared to late summer (Figs. 2a & b) ~~(Fig. 4)~~. Combined, these dynamics resulted in a much lower $\delta^{15}N\text{-}NO_3^-$ for high-latitude air masses during early summer compared to late summer (minimum value of -42.9‰ vs -25.6‰). Similarly low MBL $\delta^{15}N\text{-}NO_3^-$ values (< -30‰) were recently observed for the southern high latitudes of the Indian ocean (Shi~~,~~ et al., 2021). Our data are also consistent with ~~previous~~ year-round studies of atmospheric NO_3^- at coastal Antarctica ~~(Savarino, et al., 2007)~~(Savarino et al., 2007) and the South Pole ~~(Walters, et al., 2019)~~(Walters et al., 2019), where $\delta^{15}N\text{-}NO_3^-$

was reported to range from -46.9‰ to 10.8‰ and from -60.8‰ to 10.5‰, respectively. Both studies observed a seasonal cycle in $\delta^{15}N\text{-}NO_3^-$ whereby the lowest values occurred during sunlit periods (i.e., summer) due to snowpack NO_x emissions and the highest values occurred during dark periods (i.e., winter) due to stratospheric inputs ~~(Savarino, et al., 2007; Walters, et al., 2019)~~(Savarino et al., 2007; Walters et al., 2019).

4.2.2) Low- to Mid-latitudes: Oceanic NO_x source

At the northern extent of our transects, the low-latitude aerosol samples, defined as those with air mass back trajectories originating from anywhere north of 43° S in early summer and 41° S in late summer (Fig. 2~~4, light orange~~), had the highest average $\delta^{15}N\text{-}NO_3^-$ signature (-4.9 ± 1.3‰; n = 5). These values can be attributed to lightning-generated NO_x, which has a $\delta^{15}N$ signature close to 0‰ ~~(Hoering, 1957)~~ (Hoering 1957). Lightning activity at the low latitudes is also consistent with the higher atmospheric $[NO_3^-]$ observed (Fig. 1a~~A~~) and is further supported by co-occurring high $[NO_3^-]$ and relatively high $\delta^{15}N\text{-}NO_3^-$ (Fig. S2). An average atmospheric $\delta^{15}N\text{-}NO_3^-$ signature of -4‰ was previously reported for the low latitude Atlantic Ocean, between 45° S and 45° N, and similarly attributed to a combination of natural NO_x sources including lightning ~~(Morin, et al., 2009)~~(Morin et al., 2009).

Aerosol samples across the mid-latitudes had an average $\delta^{15}N\text{-}NO_3^-$ of -13.2‰ (Figs. 1b~~B~~ & 2). Mid-latitude air masses are defined as those originating from anywhere south of 43° S in early summer and south of 41° S in late summer that made no contact with Antarctica or any surrounding sea ice (Fig. 2a & b~~4, dark orange~~), therefore these samples were unlikely to be influenced by snow emitted NO_x with its light isotopic signature. The beginning of the mid-latitude zone (i.e., ~~end of the low-latitude zone~~43°S and 41°S in early and late summer, respectively)~~)~~ was defined by the presence of non-zero sea surface nitrite concentrations in early and late summer (Fig. 4~~5~~). However, the observed aerosol $\delta^{15}N\text{-}NO_3^-$ was too low (-14.5‰ to -11.2‰) to be explained solely by lightning generated NO_x. In the absence of any signature of anthropogenic NO_x emissions (~~see~~ Sect. 4.1), we argue that the dominant NO_x source for the mid-latitude samples originates from seawater.

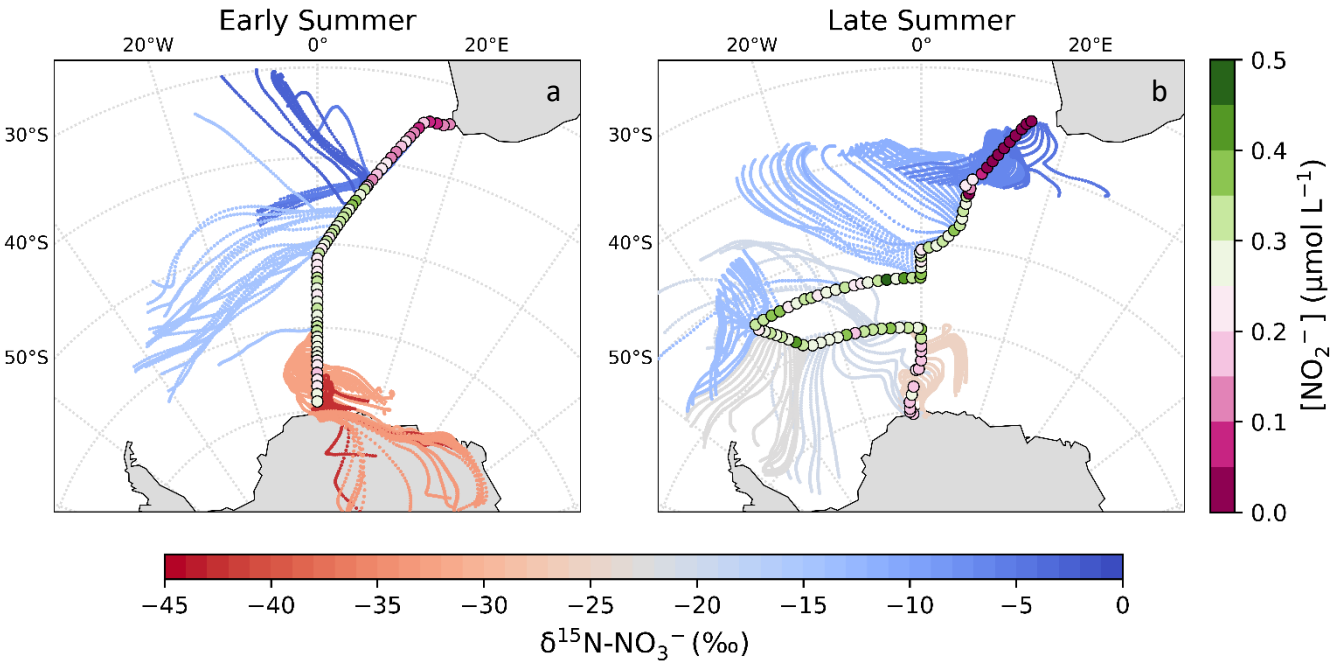

Figure~~.~~ ~~4~~5. 72-hour AMBT~~'~~s computed for each hour of the voyage during early (a~~A~~) and late (b~~B~~) summer, when the HV-AS was operational for more than 45 minutes of the hour. AMBT~~'~~s are colour coded by the weighted average $\delta^{15}N$ of atmospheric nitrate ($\delta^{15}N\text{-}NO_3^-$), represented by the horizontal colour bar. Over-layered are the surface ocean nitrite concentrations (circles; $[NO_2^-]$; µmol L^{-1}), measured along each transect and represented by the vertical colour bar.

As mentioned in section 1, the most likely mechanism for an oceanic NO_x source is via the photolysis of surface ocean derived $RONO_2$ in the MBL. NO derived from seawater nitrite is thought to limit $RONO_2$ production (D~~d~~ahl and~~&~~ Saltzman 2008; Dahl et al., 2012), such that non-zero nitrite concentrations are required for $RONO_2$ production to occur. Here, surface ocean nitrite concentrations were relatively high, in particular from ~ 41° S to 50° S (Fig. ~~4~~5). Furthermore, the latitudinal extent of mid-latitude air masses with low $\delta^{15}N\text{-}NO_3^-$ signatures corresponds well with the same latitudinal extent in which non-zero surface ocean nitrite concentrations occurred (Fig~~s~~. 4 ~~and 5~~). As such, we suggest that in this region oceanic $RONO_2$ emission is the main source to the Southern Ocean MBL, ultimately resulting in the low $\delta^{15}N\text{-}NO_3^-$ values observed for mid-latitude air masses.

No estimates exist for the $\delta^{15}N$ of oceanic $RONO_2$, however $RONO_2$ photolysis may yield isotopically light NO_x given that NO_3^- photolysis produces low $\delta^{15}N$ products (e.g., Frey et al., 2009). Therefore, once oxidised in the overlying atmosphere, NO_x derived from oceanic $RONO_2$ photolysis may form atmospheric NO_3^- with a low $\delta^{15}N$ signature. Aerosol $\delta^{15}N\text{-}NO_3^-$ values have been observed to range from -14.1‰ to -7.3‰ in the eastern equatorial Pacific ~~(Kamezaki, et al., 2019)~~(Kamezaki et al., 2019) and from -6‰ to ~0‰ (average = -3.4‰) in the western equatorial Pacific (Shi~~,~~ et al., 2021). Observed $\delta^{15}N\text{-}NO_3^-$ is higher in the western compared the eastern equatorial Pacific, which could be attributed to the proximity of the western equatorial Pacific to continental/anthropogenic NO_x sources, resulting in NO_3^- having a higher $\delta^{15}N$ signature. The low average $\delta^{15}N\text{-}NO_3^-$ observed for the mid-latitude air masses of the Southern Ocean MBL sampled in the present study (-14.5‰ to -11.2‰), are remarkably similar to those observed in the eastern equatorial Pacific (Kamazaki~~,~~ et al., 2019). Kamezaki et al., (2019) also concluded that such low $\delta^{15}N\text{-}NO_3^-$ values cannot be explained solely by lightning NO_x and given the lack of considerable influence from any continental NO_x sources, they invoked the contribution of oceanic N emissions in the form of ammonia (NH_3) and/or $RONO_2$. However, NH_3 flux data for the summertime Atlantic Southern Ocean derived from in situ ocean/atmosphere observations suggest that the ocean in this region is a net sink of NH_3 (Altieri~~,~~ et al., 2021).

The latitudinal extent of our sampling campaign enabled us to estimate a range of likely values for the N isotopic composition of NO_3^- derived from oceanic $RONO_2$. We split the latitudinal transect into three regions, each characterised by the dominance of a different natural source of NO_3^-~~-~~, i.e., lightning NO_x at the low-latitudes (Fig. 5 light orange), oceanic $RONO_2$ emissions at the mid-latitudes (Fig. 5 dark orange) and snowpack emissions at the high-latitudes (Fig. 5 red).

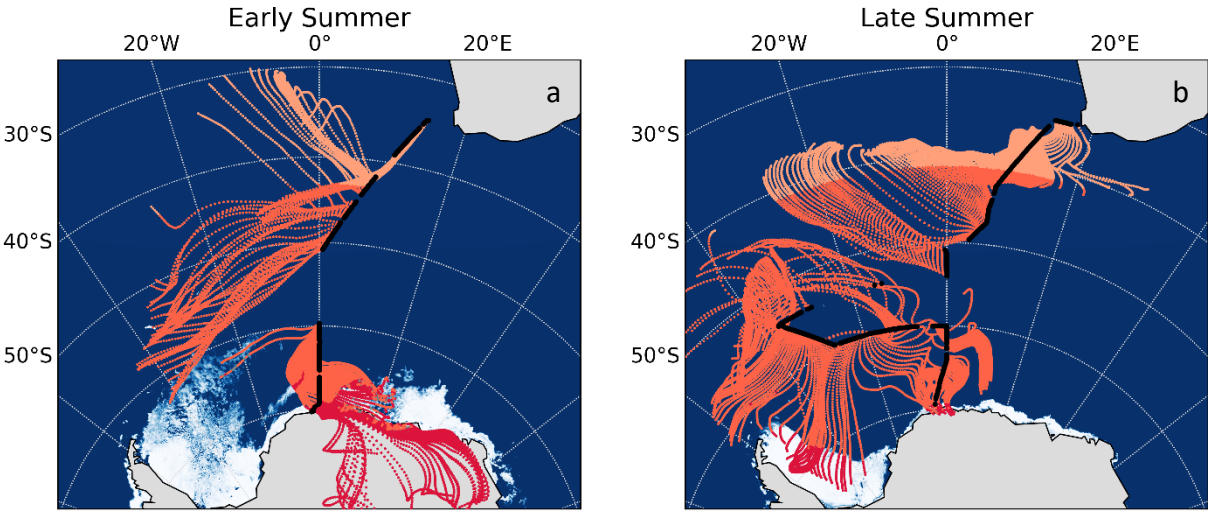

Figure~~.~~ 5. 72-hour AMBTs computed for each hour of the voyage during early (a) and late (b) summer, when the HV-AS was operational for more than 45 minutes of the hour. Light orange, dark orange and red AMBTs represent time spent over the low, mid- and high latitude SO, respectively. The white represents the location of the sea ice (see Fig. 2 caption).

Assuming that the dominant natural source of NO_3^- is the only source relevant in each latitudinal zone, we estimate the contribution of each source to total NO_3^- formation by ascertaining the amount of time air masses spent in each zone. We further assume that atmospheric $\delta^{15}N\text{-}NO_3^-$ reflects at most a combination of two sources based on the AMBTs of each sample, either lightning NO_x and oceanic $RONO_2$ emissions near South Africa, or oceanic $RONO_2$ emissions and snowpack NO_x emissions near Antarctica (Fig. 5~~4~~ and Table S6~~4~~). Using a two-end member mixing model the $\delta^{15}N$ signature of the source NO_3^- derived from mid-latitude Southern Ocean $RONO_2$ emissions was calculated for all samples where air masses from the mid-latitude region contributed at least 10% (Table S6~~4~~). This 10% threshold was chosen as the isotopic endmember of oceanic $RONO_2$ is harder to determine with confidence when its contribution to total NO_3^- is less than 10%. As an~~For~~ example, the AMBT~~'~~s for sample ES 4 spent 3% of the time in the low-latitude zone and 97% in the mid-latitude zone. Using the measured $\delta^{15}N\text{-}NO_3^-$ for ES 4 of -14.5‰ and~~Therefore,~~ assuming lightning NO_x has a $\delta^{15}N$ signature of 0‰~~ and the measured $\delta^{15}N\text{-}NO_3^-$ for ES 4 is -14.5‰~~, we calculate the $\delta^{15}N$ signature of the $RONO_2$-derived NO_3^- to be -14.9‰. It is important to note that using this approach to estimate the $\delta^{15}N\text{-}NO_3^-$ from oceanic $RONO_2$ emissions relies heavily on AMBTs generated using HYSPLIT. While HYSPLIT is a frequently used tool for assessing air mass origin in the Southern Hemisphere and over Antarctica (Morin et al., 2008; Walters et al., 2019; Shi et al., 2021), it is important to note that a spatial uncertainty of 15% to 30% of the trajectory path distance can be expected (Scarchilli et al., 2011). AMBTs also become increasingly uncertain the further back in time they are used (Sinclair et al., 2013). Some of this uncertainty is alleviated by the fact that the AMBTs generated here are relatively short (< 5 days). Additionally, the spatial scale of the low-, mid- and high-latitude zones is large, such that some variation in sample AMBTs will not significantly alter the expected dominant NO_3^- source."

Using this approach for each filter deployment along the latitudinal transect, an average $\delta^{15}N\text{-}NO_3^-$ from oceanic $RONO_2$ emissions of -2~~1~~2.~~8~~0 ± 7.~~6~~5‰ was estimated. Furthermore, the contribution of $RONO_2$ emissions can explain the lowering of $\delta^{15}N$ from 0‰ for the low-latitude air mass samples. For example, the highest $\delta^{15}N$ observed in the study was -2.7‰, and this sample has a < 5% contribution from the mid-latitude zone. The other two low-latitude samples have 30% to 40% contribution from the mid-latitude zone and their $\delta^{15}N$ is lower (Table S3), as expected due to the influence of $RONO_2$ emissions.

The influence of low $\delta^{15}N\text{-}NO_3^-$ from $RONO_2$ emissions is not limited to the Southern Ocean, and this estimate of the N isotopic composition for the $RONO_2$ derived NO_3^- source may be useful to constrain the contribution of $RONO_2$ emissions to NO_3^- formation in other ocean regions with elevated surface ocean nitrite concentrations, such as the tropical Pacific.

4.3) The O isotopes of atmospheric nitrate

The corresponding $\delta^{18}O$ values allow us to determine the pathways of NO_3^- formation from NO_x. However, an assumption must first be made regarding the oxidation of NO to NO_2. While the dominant oxidant of NO to NO_2 is O_3 (R1) in most of the troposphere, over the open ocean there can be a significant contribution via the reaction of NO with peroxy radicals (HO_2 and its organic homologues RO_2) (Alexander et al., 2020). Peroxy radicals compete with O_3 to convert NO into NO_2 via R10:

$$NO + HO_2 \text{ (or } RO_2) \rightarrow NO_2 + OH \text{ (or RO)} \quad \text{(R10)}$$

The $\delta^{18}O$ of peroxy radicals is much lower than that of O_3 because the O atoms derive from atmospheric O_2, which has a well-defined $\delta^{18}O$ of 23.9‰ ~~(Kroopnick & Craig, 1972)~~(Kroopnick and Craig, 1972). The $\delta^{18}O\text{-}NO_2$ can then be calculated using Eq.~~equation~~ (2),

$$\delta^{18}O\text{-}NO_2 = (\delta^{18}O\text{-}O_2)(1\text{-}f) + (\delta^{18}O\text{-}O_3^*)(f) \quad (2)$$

where f is the fraction of NO_2 formed from R1, (1-f) is the fraction formed from R10, and the terminal $\delta^{18}O\text{-}O_3$ value ($\delta^{18}O\text{-}O_3^*$) is 130.4 ± 12.9‰ (Vicars and~~&~~ Savarino, 2014).

The $\delta^{18}O\text{-}NO_3^-$ is then determined using Eq.~~equation~~ (3) in which two thirds of the O atoms in NO_3^- come from NO_2 and one third comes from OH i.e., R3, or using Eq.~~equation~~ (4) in which three sixths of the O atoms in NO_3^- come from O_3, two sixths come from NO_2 and one sixth comes from H_2O i.e., R4-R6 (Hastings~~,~~ et al., 2003; Alexander~~,~~ et al., 2020).

$$\delta^{18}O\text{-}NO_3^-{}_{(R3)} = (2/3)(\delta^{18}O\text{-}NO_2) + (1/3)(\delta^{18}O\text{-}OH) \quad (3)$$

$$\delta^{18}O\text{-}NO_3^-{}_{(R4\text{-}R6)} = (1/2)(\delta^{18}O\text{-}O_3^*) + (1/3)(\delta^{18}O\text{-}NO_2) + (1/6)(\delta^{18}O\text{-}H_2O) \quad (4)$$

We assume that 15% of NO to NO_2 conversion occurs via HO_2/RO_2 oxidation and 85% by O_3 oxidation as is suggested by global models (Alexander~~,~~ et al., 2020), and use the minimum and maximum $\delta^{18}O\text{-}H_2O$ range of -27.5‰ to 0‰, the temperature-dependent equilibrium isotope exchange between OH and H_2O (Walters and~~&~~ Michalski, 2016), and the resulting minimum and maximum estimates for $\delta^{18}O\text{-}OH$ of -67.4‰ to -41.0‰. Using these assumptions and Eq.~~equations~~ (3) and (4), the expected $\delta^{18}O\text{-}NO_3^-$ for the daytime OH oxidation pathway (R3) is 46.5‰ to 71.4‰, and for the dark reactions (R4-R6) is 88.7‰ to 113.5‰. The observed $\delta^{18}O\text{-}NO_3^-$ values were all less than 70‰ (Figs. 1c~~C~~ and 3), suggesting that NO_x oxidation by OH (R3) was indeed the dominant pathway for atmospheric NO_3^- formation during summer. The low $\delta^{18}O\text{-}NO_3^-$ values observed suggest a minimal influence of O_3 in the oxidation chemistry, ruling out both the halogen (R8 to R9) and DMS (R7) related NO_3^- formation pathways in addition to N_2O_5 hydrolysis (R4-6). This is consistent with previous year-round studies of atmospheric NO_3^- at coastal Antarctica ~~(Savarino, et al., 2007)~~(Savarino et al., 2007) and the South Pole ~~(Walters, et al., 2019)~~ (Walters et al., 2019) where $\delta^{18}O\text{-}NO_3^-$ was at a minimum in summer (59.6‰ and 47.0‰, respectively). Both studies confirm the importance of HO_x oxidation chemistry in summer when solar radiation enhances the production of these oxidants, followed by a switch to O_3 dominated oxidation chemistry in winter ~~(Savarino, et al., 2007; Ishino, et al., 2017; Walters, et al., 2019)~~(Savarino et al., 2007; Ishino et al., 2017; Walters et al., 2019).

Interestingly, most aerosol samples have a $\delta^{18}O\text{-}NO_3^-$ less than 46.5‰ (n=19), the lower limit estimated above for the OH pathway. This suggests that there is more NO to NO_2 conversion via HO_2/RO_2 oxidation occurring than the global average. A maximum HO_2/RO_2 contribution to NO oxidation of ~63% is required to explain the lowest $\delta^{18}O\text{-}NO_3^-$ value, which was observed over the mid-latitudes during early summer. Increased RO_2 production over the mid-latitudes could derive from $RONO_2$ photolysis in the MBL, which we hypothesise is happening in this region based on the $\delta^{15}N\text{-}NO_3^-$ (Sect.~~ion~~ 4.2.2). Although the lowest $\delta^{18}O$ observation occurred in the mid-latitudes, the majority of low $\delta^{18}O\text{-}NO_3^-$ values were observed in the Weddell Sea, away from the region of maximum $RONO_2$ emissions. Approximately half of the Weddell Sea samples have a $\delta^{18}O\text{-}NO_3^- < 31‰$, which would require a HO_2/RO_2 contribution to NO oxidation upwards of 40% (more than double the contribution estimated by global models (Alexander~~,~~ et al., 2020)). These $\delta^{18}O\text{-}NO_3^-$ observations are unusually low compared

to previous observations for the same region in spring ~~(Morin, et al., 2009)~~(Morin et al., 2009). We hypothesize that the large contribution of HO_2/RO_2 to NO/NO_2 oxidation (i.e., a decrease in f in Eq.~~equation~~ (2)) resulting in these low $\delta^{18}O\text{-}NO_3^-$ values is due to the influence of sea ice emissions. The 72-hour AMBTs for these low $\delta^{18}O\text{-}NO_3^-$ Weddell Sea samples indicate that all the air masses either originated from, or spent a significant amount of time recirculating, over the sea ice covered region of the western Weddell Sea (Fig. 6b~~A~~). By contrast, aerosol samples from the Weddell Sea with $\delta^{18}O\text{-}NO_3^-$ values greater than 31‰ have air masses that experienced significantly more oceanic influence (Fig. 6a~~A~~). There is evidence that sea ice can lead to enhanced peroxy radical production (Brough et al., 2019). In that work, increased $HO_2 + RO_2$ concentrations were observed during spring at a coastal Antarctic site when air masses arrived from across a sea ice covered zone. This was attributed to the oxidation of hydrocarbons by chlorine atoms, which leads to increased RO_2 concentrations via R11 and R12:

$$RH + Cl \rightarrow R + HCl~~I.~~ \quad \text{(R11)}$$

$$R + O_2 \rightarrow RO_2 \quad \text{(R12)}$$

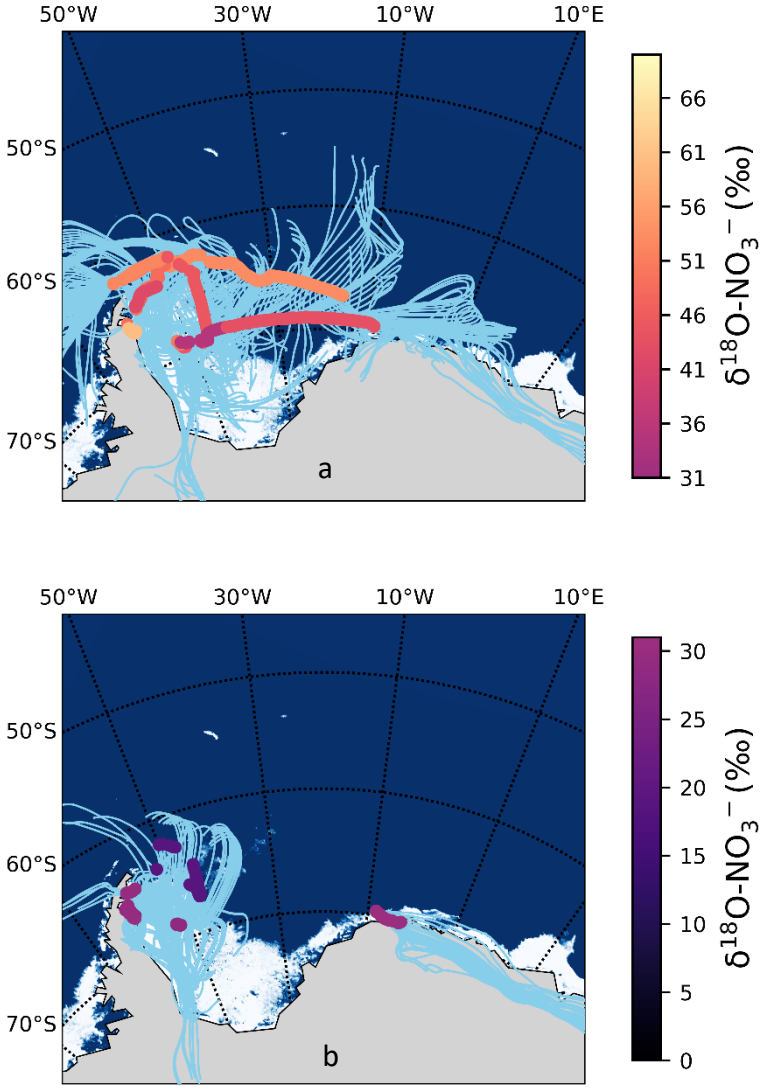

554 Figure. 6. 72-hour AMBTs (light blue ~~dashed~~ lines) computed for each hour of the voyage in the Weddell Sea, when the
555 HV-AS was operational for more than 45 minutes of the hour. The vertical colour bar represents the weighted average $\delta^{18}O$ of
556 atmospheric nitrate ($\delta^{18}O\text{-}NO_3^-$), where $\delta^{18}O\text{-}NO_3^-$ was > 31‰ (aA) and < 31‰ (bB). The white represents the location of the
557 sea ice (see Fig. 2 caption). ~~The horizontal colour bar represents satellite-derived sea ice concentration (%) for the 15th of~~
558 ~~January 2019, which corresponds to midway through the WS sampling period. Satellite-derived sea ice concentration was~~
559 ~~obtained from the AMSR2 ASI programme.~~
560
561 Cl atoms are much more reactive with hydrocarbons than OH (Monks, 2005) and can enhance hydrocarbon oxidation even
562 when present at low concentrations. Brough et al. (2019) suggest that air masses that traversed the sea ice zone contained

photolabile chlorine compounds that built up at night until photolysis occurred during the next day ~~(Brough, et al., 2019)~~(Brough et al., 2019). Although our study was conducted in summer (the season of minimum sea ice extent), the sampling locations were uniquely positioned at the western edge of the Weddell Sea gyre where significant sea ice remained (Fig. 6). Therefore, we suggest that chlorine chemistry over the sea ice increased RO_2 concentrations at the time of our sampling, allowing the NO + RO_2 pathway to play a more significant role in the Weddell Sea and resulting in low $\delta^{18}O\text{-}NO_3^-$ values. We note that the only other estimates of $\delta^{18}O\text{-}NO_3^-$ from the Weddell Sea ranged from ~ 50‰ to 110‰ during springtime, and these samples were associated with air masses that spent almost no time over the sea ice and therefore had limited potential for this peroxy radical chemistry to drive down the $\delta^{18}O\text{-}NO_3^-$ to the low values we observe~~d (Morin, et al., 2009)~~ (Morin et al., 2009).

5) Conclusions

Our observations across a large latitudinal gradient of the summertime Southern Ocean MBL suggest it is dominated by natural NO_x sources with distinct~~unique~~ isotopic signatures. Aerosol NO_3^- was predominantly formed from lightning generated NO_x with a $\delta^{15}N$ of ~ 0‰ at the lower latitudes, whereas snowpack NO_x emissions with a $\delta^{15}N$ ~ -48‰ dominated the MBL inventory at higher latitudes. Over the mid-latitudes, NO_3^- derived primarily from oceanic $RONO_2$ emissions, with an estimated $\delta^{15}N$ signature of ~ -22.0‰. Additional research is needed to improve our mechanistic and isotopic understanding of surface ocean $RONO_2$ formation, flux, and conversion to aerosol nitrate in order to constrain~~This estimate may be valuable in constraining~~ the contribution of oceanic $RONO_2$ emissions to NO_3^- formation in other ocean regions where this source has been invoked, such as the tropical Pacific (Kamezaki et al., 2019). The isotopic composition of NO_3^- observed here can further inform interpretations of Antarctic ice core NO_3^- isotope records to understand aerosol climate forcing and controls on the atmospheric oxidation budget over millennia ~~(Freyer, et al., 1996; Jiang, et al., 2019)~~(Freyer et al., 1996; Jiang et al., 2019) – the interpretation of which relies on knowledge of the NO_x isotopic source signatures in the polar atmosphere.

The $\delta^{18}O\text{-}NO_3^-$ values were consistently lower than 70‰, which confirms NO_x oxidation by OH (R3) to be the dominant pathway for atmospheric NO_3^- formation during summer. However, unusually low $\delta^{18}O\text{-}NO_3^-$ values observed at the mid-latitudes and in the Weddell Sea indicate the increased importance of peroxy radicals (and decreased importance of O_3) in NO oxidation to NO_2 in the MBL~~.~~ At the mid -latitudes peroxy radicals (RO_2) may derive from -$RONO_2$ photolysis~~ in the MBL~~, while i~~I~~n the Weddell Sea, sea ice appears to play an important role in the formation of this oxidant via its influence on chlorine chemistry ~~in the MBL~~ (Brough~~,~~ et al., 2019). This implies that snow covered sea ice is not only a source of NO_x but also other species that have the potential to change the composition of the atmosphere above the ice and impact NO_x oxidation chemistry. These results also highlight the utility of $\delta^{18}O\text{-}NO_3^-$ to identify the major oxidants in NO oxidation, as well as NO_x to NO_3^- conversion. In particular, $\delta^{18}O\text{-}NO_3^-$ can serve as a useful tool for testing our understanding of the relative importance of HO_2/RO_2 in NO/NO_2 cycling, which can be difficult to constrain in some environments.

Our study challenges the traditional paradigm that considers the ocean as a passive recipient of N deposition, as the Southern Ocean mid-latitude NO_3^- source may derive almost entirely from oceanic $RONO_2$ emissions. In the tropical equatorial Pacific atmosphere, Kamezaki et al. (2019) also suggested evidence for a low $\delta^{15}N\text{-}NO_3^-$ source derived from the ocean. In the subtropical Atlantic Ocean MBL, Altieri et al. (2016) found that biogeochemical cycling in the surface ocean can directly influence the lower atmosphere serving as a source of aerosol organic N and ammonium. This study suggests that the surface waters of the Southern Ocean may also serve as a NO_x source, ultimately resulting in NO_3^- aerosol formation. As such, the surface ocean may play a bigger role in atmospheric oxidative capacity over remote marine regions than previously thought.

Author contributions. K.E.A designed the study and sampling campaign, acquired funding and supervised the research. K.E.A and J.G. provided financial and laboratory resources and assisted in data validation. K.A.M.S. and J.M.B conducted the sampling at-sea and J.M.B. performed the laboratory analyses. M.G.H and E.J. assisted in data validation, reviewing, and editing the manuscript. J.M.B analysed the data and prepared the manuscript with contributions from all co-authors.

Competing interests. The authors declare that they have no conflict of interest.

Data availability statement. Data sets for this research are available at https://doi.org/10.5281/zenodo.5740618. ~~10.5281/zenodo.5006983~~

Acknowledgements. We thank the Captain and crew of the R/V *SA Agulhas II* for their support at sea and the Marine Biogeochemistry Lab in the Oceanography Department at the University of Cape Town for their assistance in the field and laboratory. We thank Lija Treibergs, Reide Jacksin and Peter Ruffino for their assistance in analysing the nitrate isotopes and Riesna Audh for her assistance with satellite derived sea ice concentration data. We thank Riesna Audh, Raquel Flynn and Shantelle Smith for nitrite concentration measurements, and Raquel Flynn for quality controlling the nitrite concentration data. This research was partially funded by a CAREER award to J.G. from the U.S. National Science Foundation (OCE-1554474). This research was also supported by the South African National Research Foundation through a Competitive Support for Rated Researchers Grant to K.E.A. (111716), South African National Antarctic Programme Postgraduate Fellowship to J.M.B, and Grant to K.E.A (110732); UCT support to K.E.A. through a University Research Council Launching Grant and VC Future Leaders 2030 Grant.

6) References

Alexander, B., and~~&~~ Mickley, L. J.: Paleo-perspectives on the potential future changes in the oxidative capacity of the atmosphere due to climate change and anthropogenic emissions, Curr~~ent~~ Pollution Rep~~orts~~., 1, 57-69, https://doi.org/10.1007/s40726-015-0006-0~~DOI 10.1007/s40726-015-0006-0~~, 2015.

Alexander, B., Sherwen, T., Holmes, C. D., Fisher, J. A., Chen, Q., Evans, A. J., and Kasibhatla, P.: Global inorganic nitrate production mechanisms: comparison of a global model with nitrate isotope observations. Atmos.pheric Chem.istry and Phys.ics, 20(6), 3859-3877, https://doi.org/10.5194/acp-20-3859-2020, 2020.

Altieri, K. E., Fawcett, S. E., and& Hastings, M.G.: Reactive Nitrogen Cycling in the Atmosphere and Ocean, Annu.al Rev.iew of Earth and Planet.tetary Sci.ences, 49, 513-540, https://doi.org/10.1146/annurev-earth-083120-052147, 2021.

Altieri, K. E., Fawcett, S. E., Peters, A. J., Sigman, D. M., and& Hastings, M. G.: Marine biogenic source of atmospheric organic nitrogen in the subtropical North Atlantic, PNAS., 113(4), 925-930, https://doi.org/10.1073/pnas.1516847113, 2016

Altieri, K. E., Hastings, M. G., Gobel, A. R., Peters, A. J., and& Sigman, D. M.: Isotopic composition of rainwater nitrate at Bermuda: the influence of air mass source and chemistry in the marine boundary layer, J.ournal of Geophys.ical Res.earch: Atmos.pheres, 118, 11304-11316, https://doi.org/10.1002/jgrd.50829, 2013.

Atlas, E., Pollock, W., Greenberg, J., Heidt, L., and& Thompson, A. M..: Alkyl nitrates, nonmethane hydrocarbons, and halocarbon gases over the equatorial Pacific Ocean during Saga 3, J. Geophys. Res. Atmos.ournal of Geophysical Research Letters, 98(D9), 16933-16947, https://doi.org/10.1029/93JD01005, 1993.

Baker, A. R., Lesworth, T., Adams, C., Jickells, T. D., and& Granzeveld, L.: Estimation of atmospheric nutrient inputs to the Atlantic Ocean from 50°N to 50°S based on large-scale field sampling: Fixed nitrogen and dry deposition of phosphorus, Global Biogeochem.ical Cycles, 24, GB3006, https://doi.org/10.1029/2009GB003634, 2010.

Bauguitte, A. J.-B., Bloss, W. J., Evans, M. J., Salmon, R. A., Anderson, P. S., Jones, A. E., Lee, J. D., Saiz-Lopez, A., Roscoe, H. K., Wolff, E. W., and &Plane, J. M. C.: Summertime NO_x measurements during the CHABLIS campaign: can source and sink estimates unravel observed diurnal cycles?, Atmos.pheric Chem.istry and Phys.ics, 12, 989-1002, https://doi.org/10.5194/acp-12-989-2012, 2012.

Behrenfeld, M. J., Boss, E., Siegel, D. A., and Shea, D. M.: Carbon-based ocean productivity and phytoplankton physiology from space, Global Biogeochem.ical Cycles, 19(1), 1-14, https://doi.org/10.1029/2004GB002299, 2005.

Berhanu, T. A., Meusinger, C., Erbland, J., Jost, R., Bhattacharya, S. K., Johnson, M. S., and& Savarino, J.: Laboratory study of nitrate photolysis in Antarctic snow. II. Isotopic effects and wavelength dependence, The J.ournal of Chem.ical Phys.ics, 140(244306), 1-14, https://doi.org/10.1063/1.4882899, 2014.

Berhanu, T. A., Savarino, J., Erbland, J., Vicars, W. C., Preunkert, S., Martins, J. F., and& Johnson, M. S.: Isotopic effects of nitrate photochemistry in snow: a field study at Dome C, Antarctica, Atmos.pheric Chem.istry and Phys.ics, 15, 11243-11256, https://doi.org/10.5194/acp-15-11243-2015, 2015.

Blake, N. J., Blake, D. R., & Swanson, A. L., Atlas, E., Flocke, F., and& Rowland, F. S.: Latitudinal, vertical, and seasonal variations of C_1-C_4 alkyl nitrate in the troposphere over the Pacific Ocean during PEM-Tropics A and B: Oceanic and continental sources, J. Geophys. Res. Atmos.Journal of Geophysical Research Letters, 108(D2), 1-14, https://doi.org/10.1029/2001JD001444doi:10.1029/2001JD001444, 2003.

Blake, N. J., Blake, D. R., Wingenter, O. W., Sive, B. C., Kang, C. H., Thornton, D. C., Bandy, A. R., Atlas, E., Flocke, F., Harris, J. M., and& Rowland, F. S.: Aircraft measurements of the latitudinal, vertical, and seasonal variations of NMHCs, methyl nitrate, methyl halides, and DMS during the First Aerosol Characterization Experiment (ACE 1), J. Geophys. Res. Atmos.Journal of Geophysical Research Letters, 104(D17), 21803-21817, **https://doi.org/10.1029/1999JD900238**, 1999.

Bölhke, J. K., Mroczkowski, S. J., and& Coplen, T. B.: Oxygen isotopes in nitrate: new reference materials for $^{18}O:^{17}O:^{16}O$ measurements and observations on nitrate-water equilibrium, Rapid Commun. Mass Spectrom. Rapid Communications in Mass Spectrometry, 17(16), 1835-1846, https://doi.org/10.1002/rcm.1123, 2003.

Brough, N., Jones, A. E., and& Griffiths, P. T.: Influence of sea ice-derived halogens on atmospheric HO_x as observed in Springtime coastal Antarctica, Geophys. Res. Lett.Geophysical Research Letters, 46, 10168-10176, https://doi.org/10.1029/2019GL083825, 2019.

Casado, M., Landais, A., Masson-Delmotte, V., Genthon, C., Kerstel, E., Kassi, S., Arnaud, L., Picard, G., Prie, F., Cattani, O., Steen-Larsen, H. -C., Vignon, E., and& Cermak, P.: Continuous measurements of isotopic composition of water vapour on the East Antarctic Plateau, Atmos.pheric Chem.istry and Phys.ics, 16(13), 8521-8538, https://doi.org/10.5194/acp-16-8521-2016, 2016.

Casciotti, K.L., Sigman, D.M., Hastings, M.G., Böhlke, J.K. and& Hilkert, A.: Measurement of the oxygen isotopic composition of nitrate in seawater and freshwater using the denitrifier method, Anal.ytical chem.istry, 74(19), 4905-4912, https://doi.org/10.1021/ac020113w, 2002.

Chuck, A. L., Turner, S. M., and& Liss, P. S.: Direct evidence for a marine source of C_1 and C_2 alkyl nitrates, Science, 297, 1151-1154, https://doi.org/10.1126/science.1073896, 2002.

Collett, K. S., Piketh, S. J., and Ross, K. E.: An assessment of the atmospheric nitrogen budget on the South African Highveld, S. Afr. J. Sci., 106(5/6), 1-9, http://dx.doi.org/10.4102/sajs.v106i5/6.220, 2010.

Dahl, E. E., and& Saltzman, S. E.: Alkyl nitrate photochemical production rates in North Pacific seawater, Mar.ine Chem.istry, 112, 137-141, https://doi.org/10.1016/j.marchem.2008.10.002, 2008.

Dahl, E. E., Heiss, E. M., and& Murawski, K.: The effects of dissolved organic matter on alkyl nitrate production during GOMECC and laboratory studies, Mar.ine Chem.istry, 142, 11-17, https://doi.org/10.1016/j.marchem.2012.08.001, 2012.

Dahl, E. E., Saltzman, SE. ES., and& de Bruyn, W. J.: The aqueous phase yield of alkyl nitrates from ROO + NO: Implications for photochemical production in seawater, Geophys. Res. Lett.Geophysical Research Letters, 30(6), 1-4, https://doi.org/10.1029/2002GL016811, 2003.

Dahl, E. E., Yvon-Lewis, S. A., and& Saltzman, S. E.: Saturation anomalies of alkyl nitrates in the tropical Pacific Ocean, Geophys. Res. Lett.Geophysical Research Letters, 32(L20817), 1-4, https://doi.org/10.1029/2005GL023896, 2005.

Dar, S. S., Ghosh, P., Swaraj, A., and& Kumar, A.: CGraig-Gordon model validation using observed meteorological parameters and measured stable isotope ratios in water vapor over the Southern Ocean, Atmos.spheric Chem.istry and Phy.sics Discussions, 20(19), 11435-11449, https://doi.org/10.5194/acp-20-11435-2020, 2020.

Davidson, E. A., and& Kingerlee, W.: A global inventory of nitric oxide emissions from soils, Nutr. Cycling Agroecosyst. Nutrient Cycling in Agroecosystems, 48, 37-50, https://doi.org/10.1023/A:1009738715891, 1997.

Elliott, E. M., Kendall, C., Wankel, S. D., Burns, S. A., Boyer, E. W., Harlin, K., Bain, D. J., and& Butler, T. J.: Nitrogen isotopes as indicators of NO_x source contributions to atmospheric nitrate deposition across the Midwestern and Northeastern United States,—. Environ.nmental Sci.ence and —Technol.ogy, 41(22), 7661-7667, https://doi.org/10.1021/es070898t, 2007.

Erbland, J., Vicars, W. C., Savarino, J., Morin, S., Frey, M. M., Frosini, D., Vince, E., and Martins, J. M. F.: Air-snow transer of nitrate on the East Antarctic Plateau - Part 1: Isotopic evidence for a phytolytically driven dynamic equilibrium in summer,. Atmos.pheric Chem.istry and Phys.ics, 13(13), 6403-6419, https://doi.org/10.5194/acp-13-6403-2013, 2013.

Fang, Y. T., Koba, K., Wang, X. M., Wen, D. Z., Li, J., Takebayashi, Y., Liu, X. Y., and& Yoh, M.: Anthropogenic imprints on nitrogen and oxygen isotopic composition of precipitation nitrate in a nitrooргen-polluted city in southern China,. Atmos.pheric Chem.istry and Phys.ics, 11, 1313-1325, https://doi.org/10.5194/acp-11-1313-2011, 2011.

Finlayson-Pitts, B. J., and& Pitts, J. N.: Chemistry of the upper and lower troposphere. San Diego, California: Academic Press, 2000.

Fisher, J. A., Atlas, E. L., Barletta, B., Meinardi, S., Blake, D. R., Thompson, C. R., Ryerson, T. B., Peischl, J., Tzompa-Sosa, Z. A., and& Murray, L. T.: Methyl, ethyl and propyl nitrates: global distribution and impacts on reactive nitrogen in remote marine environments, J. Geophys. Res. Atmos.Journal of Geophysical Research: Atmospheres, 123(21), 412-429, https://doi.org/10.1029/2018JD029046, 2018.

Frey, M. M., Savarino, J., Morin, S., Erbland, J., and& Martins, J. M.: Photolysis imprint in the nitrate stable isotope signal in snow and atmosphere of East Antarctica and implications for reactive nitrogen cycling, Atmos.pheric Chem.istry and Phys.ics, 9, 8681-8696, https://doi.org/10.5194/acp-9-8681-2009, 2009.

Freyer, H. D.: Seasonal variation of $^{15}N/^{14}N$ ratios in atmospheric nitrate species, Tellus B: Chem. Phys. Meteorol.Tellus B: Chemical and Physical Meterology, 43(1), 30-44, https://doi.org/10.1034/j.1600-0889.1991.00003.x, 1991.

Freyer, H. D., Kley, D., Volz-Thomas, A., and& Kobel, K.: On the interaction of isotopic exchange processes with photochemical reactions in atmospheric oxides of nitrogen, J. Geophys. Res. Atmos.Journal of Geophysical Research, 98(D8), 14791-14796, https://doi.org/10.1029/93JD00874, 1993.

Freyer, H. D., Kobel, K., Delmas, R. J., Kley, D., and& Legrand, M. R.: First results of $^{15}N/^{14}N$ ratios in nitrate from alpine and polar ice cores, Tellus B: Chem. Phys. Meteorol. Tellus B: Chemical and Physical Meterology, 48(1), 93-105, https://doi.org/10.3402/tellusb.v48i1.15671, 1996.

Gobel, A. R., Altieri, K. E., Peters, A. J., Hastings, M. G., and& Sigman, D. M.: Insights into anthropogenic nitrogen deposition to the North Atlantic investigated using the isotopic composition of aerosol and rainwater nitrate, Geophys. Res. Lett.Geophysical Research Letters, 5977-5982, https://doi.org/10.1002/2013GL058167, 2013.

Grannas, A. M., Jones, A. E., Dibb, J., Ammann, M., Anastasio, C., Beine, H. J., Bergin, M., Bottenheim, J., Boxe, C. S., Carver, G., Chen, G., Crawford, J. H., Domine, F., Frey, M. M., Guzman, M. I., Heard, D. E., Hemig, D., Hoffmass, M. R., Honrath, R. E., Huey, L. G., Hutterli, M., Jacobi, H. W., Klan, P., Lefer, B., McConnell, J., Plane, J., Sander, R., Savarino, J., Shepson, P. B., Simpson, W. R., Sodeau, J. R., von Glasow, R., Weller, R., Wolff, E. W., and& Zhu, T.: An overview of snow photochemistry: evidence, mechanisms and impacts, Atmosp.sheric Chem.istry and Phys.ics Discussions, 7(2), 4165-4283, https://doi.org/10.5194/acp-7-4329-2007, 2007.

Grasshoff, K., Kremling, K., & Ehrhardt, M.: Methods of seawater analysis, Verlag Chemi, Florida, 1983.

Guha, T., Lin, C. T., Bhattacharya, S. K., Mahajan, A. S., Ou-Yang, C.-F., Lan, Y.-P., Hsu, S. C., and& Liang, M.-C.: Isotope ratios of nitrate in aerosol samples from Mt. Lulin, a high altitude station in Central Taiwan, Atmos.pheric Environ.nmentt, 154, 53-69, http://dx.doi.org/10.1016/j.atmosenv.2017.01.036, 2017

Guilpart, E., Vimeux, F., Evan, S., Brioude, J., Mertzger, J., Barthe, C., Risi, C., and& Cattani, O.: The isotopic composition of near-surface water vapor at the MaïdoMaido observatory (Reunion Island, southwestern Indian Ocean) documents the controls of the humidity of the subtropical troposphere, J. Geophys. Res. Atmos.Journal of Geophysical Research: Atmospheres, 122, 9628-9650, https://doi.org/10.1002/2017JD026791, 2017.

Hamilton, D. S., Lee, L. A., Pringle, K. J., Reddington, C. L., Spracklen, D. V., and& Carslaw, K. S.: Occurence of pristine aerosol environments on a polluted planet, Proceedings of the National Academy of SciencesPNAS, 111(52), 18466-18471, https://doi.org/10.1073/pnas.1415440111, 2014.

Hastings, M. G., Sigman, D. M., & Lipschultz, F.: Isotopic evidence for source changes of nitrate in rain at Bermuda, J. Geophys. Res. Atmos.Journal of Geophysical Research: Atmospheres, 108(D24), https://doi.org/10.1029/2003JD003789, 2003.

Haywood, J., and& Boucher, O.: Estimates of the direct and indirect radiative forcing due to tropospheric aerosols: a review, Rev. Geophys.Reviews of Geophysics, 513-543, https://doi.org/10.1029/1999RG000078, 2000.

Hoering, T.: The isotopic composition of the ammonia and the nitrate ion in rain, Geochim. Cosmochim. Acta.Geochimica et Cosmochimica Acta, 12(1-2), 97-102, https://doi.org/10.1016/0016-7037(57)90021-2, 1957.

IPCC 2013: Boucher, O. D., Randall, P., Artaxo, C., Bretherton, G., Feingold, P., Forster, V.-M., Kerminen, Y., Kondo, H., Liao, U., Lohmann, P., Rasch, S.K., Satheesh, S., Sherwood, B., Stevens, and& Zhang, X. Y.: Clouds and Aerosols, in: Climate Change 2013: The Physical Science Basis. Contribution of Working Group I to the Fifth Assessment Report of the Intergovernmental Panel on Climate Change, edited by: Stocker, T.F., Qin, D., Plattner, G.-K., Tignor, M., Allen, S. K., Boschung, J, Nauels, A., Xia, Y., Bex, V., and& Midgley, P. M., Cambridge University Press, Cambridge, United Kingdom and New York, NY, USA, 2013.

Ishino, S., Hattori, S., Savarino, J., Jourdain, B., Preunkert, S., Legrand, M., Caillon, N., Barbero, A., Kurlbayashi, N., and& Yoshida, N.: Seasonal variations of triple oxygen isotopic compositions of atmospheric sulfate, nitrate and ozone at Durmont d'Urville, coastal Antarctica, Atmo.spheric Chem.istry and Phys.ics, 17, 3713-3727, https://doi.org/10.5194/acp-17-3713-2017, 2017.

Jacobi, H.-W., and& Schrems, O.: Peroxyacetyl nitrate (PAN) distribution over the South Atlantic Ocean, Phys. Chem. Chem. Phys.Physical Chemistry Chemical Physics, 1, 5517-5521, https://doi.org/10.1039/A905290I, 1999.

Jacobi, H.-W., Weller, R., Jones, A. E., Anderson, P. S., and& Schrems, O.: Peroxyacetyl nitrate (PAN) concentrations in the Antarctic troposphere measured during the photochemical experiment at Neumayer (PEAN'99). Atmos.pheric Environ.ment, 34, 5235-5247, https://doi.org/10.1016/S1352-2310(00)00190-4, 2000.

Jiang, S., Shi, G., Cole-Dai, J., Geng, L., Ferris, D. G., An, C., and& Li, Y.: Nitrate preservation in snow at Dome A, East Antarctica from ice core concentration and isotope records, Atmos.pheric Environ.ment, 213, 405-412, https://doi.org/10.1016/j.atmosenv.2019.06.031, 2019.

Johnston, J. C., & Thiemens, M. H.(1997):. The isotopic composition of tropospheric ozone in three environments. J. Geophys. Res. Atmos.Journal of Geophysical Research: Atmospheres, 102(D21), 25395-25404, https://doi.org/10.1029/97JD02075, 1997.

Jones, A. E., Weller, R., Anderson, P. S., Jacobi, H.-W., Wolff, E. W., Schrems, O., and& Miller, H.: Measurements of NO_x emissions from the Antarctic snowpack, Geophys. Res. Lett.Geophysical Research Letters, 28(8), 1499-1502, https://doi.org/10.1029/2000GL011956, 2001.

Jones, A. E., Weller, R., Minikin, A., Wolff, E. W., Sturges, W. T., McIntyre, H. P., Leonard, S. R., Schrems, O., and& Bauguitte, S.: Oxidized nitrogen chemistry and speciation in the Antarctic troposphere, J. Geophys. Res. Atmos.Journal of Geophysical Research, 104(D17), 21355-21366, https://doi.org/10.1029/1999JD900362, 1999.

Jones, A. E., Weller, R., Wolff, E. W., and& Jacobi, H.-W.: Speciation and rate of photochemical NO and NO_2 production in Antarctic snow, Geophys. Res. Lett.Geophysical Research Letters, 27(3), 345-348, https://doi.org/10.1029/1999GL010885, 2000.

Kamezaki, K., Hattori, S., Iwamoto, Y., Ishino, S., Furutani, H., Miki, Y., Uematsu, M., Miura, K., and& Yoshida, N.: Tracing the sources and forromation pathways of atmospheric particulate nitrate over the Pacific Ocean using stable isotopes, Atmos.pheric Environ.ment , 209, 152-166, https://doi.org/10.1016/j.atmosenv.2019.04.026, 2019.

Kendall, C., Elliot, E. M., and& Wankel, S. D.: Tracing anthropogenic inputs of nitrogen to ecosystems, in: Stable isotopes in ecology and environmental science, edited by: Michener, R., & Lajtha, K., Blackwell Publishing, Malden, Mass 375-449, https://doi.org/10.1002/9780470691854.ch12, 2007.

Kim, M. J., Michaud, J. M., Williams, R., Sherwood, B. P., Pomeroy, R., Azam, F., Burkart, M., and& Bertram, T. H.: Bacteria-driven production of alkyl nitrates in seawater, Geophys. Res. Lett.Geophysical Research Letters, 42, 597-604, https://doi.org/10.1002/2014GL062865, 2015.

Krankowsky, D., Bartecki, F., Klees, G. G., Mauersberger, K., and& Schellenbach, K.: Measurement of heavy isotope enrichment in tropospheric ozone, Geophys. Res. Lett.Geophysical Research Letters, 22(13), 1713-1716, https://doi.org/10.1029/95GL01436, 1995.

Kroopnick, P., and& Craig, H.: Atmospheric oxygen: isotopic composition and solubility fractionation, Science, 175(4017), 54-55, 1972.

Lee, H.-M., Henze, D. K., Alexander, B., and& Murray, L. T.: Investigating the sensitivity of surface-level nitrate seasonality in Antarctica to primary sources using a global model, Atmos.pheric Environ.ment, 89, 757-767, http://dx.doi.org/10.1016/j.atmosenv.2014.03.003, 2014.

Michalski, G., Bhattacharya, S. K., and& Mase, D. F.: Oxygen isotope dynamics of atmospheric nitrate and its precursor molcules, in: Handbook of environmental isotope geochemistry. Advances in Isotope Geochemistry, edited by: Baskaran, M., Springer, Berlin, Heidelberg, 613-635, https://doi.org/10.1007/978-3-642-10637-8_30, 2012.

Michalski, G., Scott, Z., Kabiling, M., and& Thiemens, M. H.: First measurments and modeling of $\Delta^{17}O$ in atmospheric nitrate, Geophys. Res. Lett.Geophysical Research Letters, 30(9), https://doi.org/10.1029/2003GL017015, 2003.

Monks, P. S.: Gas-phase radical chemistry in the troposphere, Chem.ical Soc.iety Rev.iews, 34, 376-395, https://doi.org/10.1039/B307982C DOI: 10.1039/b307982c, 2005.

Morin, S., Savarino, J., Frey, M. M., Domine, F., Jacobi, H. W., Kaleschke, L., and& Martins, J. M.: Comprehensive isotopic composition of atmospheric nitrate in the Atlantic Ocean boundary layer from 65°S to 79°N, J. Geophys. Res. Atmos.Journal of Geophysical Research, 114(D05303), 1-19, https://doi.org/10.1029/2008JD010696, 2009.

Nadzir, M. S., Ashfold, M. J., Khan, M. F., Robinson, A. D., Bolas, C., Latif, M. T., Wallis, B. M., Mead, M. I., Hamid, H. H. A., Harris, N. R. P., Ramly, Z. T. A., Lai, G. T., Liew, J. N., Ahamed, F., Uning, R., Samah, A. A., Maulud, K. N., Suparta, W., Zainudin, S. K., Wahab, M. I. A., Sahani, M., Müller Muller, M., Yeok, F. S., Rahman, N. A., Mujahid, A., Morris, K. I. and& Sasso, N. D.: Spatial-temporal variations in surface ozone over Ushuaia and the Antarctic region: observations from in situ measurements, satellite data, and global models, Environ. Sci. Pollut. Res. Environmental Science and Pollution Research, 25, 2194-2210, https://doi.org/10.1007/s11356-017-0521-1, 2018.

Nesbitt, S. W., Zhang, R., and& Orville, R. E.:Seasonal and global NO_x production by lightning estimated from the Optical Transient Detector (OTD), Tellus B: Chem. Phys. Meteorol.Chemical and Physical Meteorology, 52(5), 1206-1215, https://doi.org/10.3402/tellusb.v52i5.17098, 2000.

Park, S. S., and& Kim, Y. J.: Source contributions to fine particulate matter in an urban atmosphere, Chemosphere, 59, 217-226, https://doi.org/10.1016/j.chemosphere.2004.11.001, 2005.

Park, Y., Park, K., Kim, H., Yu, S., Noh, S., Kim, M.-S, Kim, J.-Y., Ahn, J.-Y., Seok, K.-S., and& Kim, Y.-H.: Characterizing isotopic compositions of TC-C, $NO3^-$-N and $NH4^+$-N in $PM_{2.5}$ in South Korea: Impact of China's winter heating, Environ.mental Pollut.ion, 233, 735-744, https://doi.org/10.1016/j.envpol.2017.10.072, 2018.

Rolph, G.D.: Real-time Environmental Applications and Display System (READY) Website (http://www.ready.noaa.gov). NOAA Air Resources Laboratory, College Park, MD, 2016.

Savarino, J., Kaiser, J., Morin, S., Sigman, D. M., and& Thiemens, M. H.: Nitrogen and oxygen isotopic constraints on the origin of atmospheric nitrate in coastal Antarctica, Atmos.pshere Chem.istry and Phys.ics, 7, 1925-1945, https://doi.org/10.5194/acp-7-1925-2007, 2007.

Scarchilli, C., Frezzotti, M., and Ruti, P. M.: Snow precipitation at four ice core sites in East Antarctica: provenance, seasonality and blocking factors, Clim. Dyn. 37, 2107-2125, https://doi.org/10.1007/s00382-010-0946-4, 2011.

Schumann, U., and& Huntrieser, H.: The global lightning induced nitrogen oxides source, Atmos.pheric Chem.istry and Phys.ics Discussions, 7(1), 2623-2818, https://doi.org/10.5194/acp-7-3823-2007, 2007.

Shi, G., Buffen, A. M., Hastings, M. G., Li, C., Ma, H., Li, Y., Sun, B., An, C., and& Jiang, S.: Investigating the post-depositional processing of nitrate in East Antarctic snow: isotopic contraints in photolytic loss, re-oxidation, and source inputs, Atmos.pheric Chem.istry and Phys.ics, 15, 9435-9453, https://doi.org/10.5194/acp-15-9435-2015, 2015.

Shi, G., Buffen, A. M., Ma, H., Hu, Z., Sun, B., Li, C., Yu, J., Ma, T., An, C., Jiang, S., Li, Y., and& Hastings, M. G.: Distinguishing summertime atmopsheric production of nitrate across the East Antarctic ice sheet, Geochim. Cosmochim. Acta.Geochimica et Cosmochimica Acta, 231, 1-14, https://doi.org/10.1016/j.gca.2018.03.025, 2018.

Shi, G., Ma, H., Zhu, Z., Hu, A., Chen, Z., Jiang, Su., An, C., Yu, J., Ma, T., Li, Y., Sun, B., and Hastings, M. G.: Using stable isotopes to distinguish atmospheric nitrate production and its contribution to the surface ocean across hemispheres, Earth Planet. Sci. Lett.Earth and Planetary Science Letters, 564, 1-12, https://doi.org/10.1016/j.epsl.2021.116914, 2021.

Sigman, D.M., Casciotti, K.L., Andreani, M., Barford, C., Galanter, M.B.J.K. and& Böhlke, J.K.: A bacterial method for the nitrogen isotopic analysis of nitrate in seawater and freshwater, Anal.ytical Cehem.istry, 73(17), 4145-4153, https://doi.org/10.1021/ac010088e, 2001.

Sinclair, K. E., Bertler, N. A. N., Trompetter, W. J., and Baisden, W. T.: Seasonality of airmass pathways to coastal Antarctica: ramifications for interpreting high-resolution ice core records, J. Clim., 26(6), 2065-2076, https://doi.org/10.1175/JCLI-D-12-00167.1, 2013.

Spreen, G., Kaleschke, L., and& Heygster, G.: Sea ice remote sensing using AMSR-E 89-GHz channels, J. Geophys. Res. Oceans Journal of Geophysical Research: Oceans, 113(C02S03), 1-14, https://doi.org/10.1029/2005JC003384, 2008.

Stein, A.F., Draxler, R.R, Rolph, G.D., Stunder, B.J.B., Cohen, M.D., and& Ngan, F.: NOAA's HYSPLIT atmospheric transport and dispersion modeling system, Bull. Amer. Meteor. Soc., 96, 2059-2077, https://doi.org/10.1175/BAMS-D-14-00110.1, 2015.

Thiemens, M. H.: History and applications of mass-independent isotope effects. Annu. Rev. Earth Planet. Sci.Annual Review of Earth and Planetary Sciences, 34, 217-262, https://doi.org/10.1146/annurev.earth.34.031405.125026, 2006.

van der A, R. J., Eskes, H. J., Boersma, K. F., van Noije, T. P., Van Roozendael, M., De Smedt, I., Peters, D. H. M. U., and& Meijer, E. W.: Trends, seasonal variability and dominant NO_x source derived from a ten year record of NO_2 measured from space, J. Geophys. Res. Atmos.Journal of Geophysical Research, 113, 1-12, https://doi.org/10.1029/2007JD009021, 2008.

Vicars, W. C., and Savarino, J.: Quantitative constraints on the ^{17}O-excess ($\Delta^{17}O$) signature of surface ozone: Ambient measurements from 50°N to 50°S using the nitrite-coated filter technique,. Geochim. Cosmochim. Acta.Geochimica et Cosmochimica Acta, 135, 270-287, https://doi.org/10.1016/j.gca.2014.03.023, 2014.

Virkkula, A., Teinila, K., Hillamo, R., Kerminen, V. M., Saarikoski, S., Aurela, M., Viidanoja, J., Paatero, J., Koponen, I. K., and& Kulmala, M.: Chemical composition of boundary layer aerosol over the Atlantic Ocean and at an Antarctic site, Atmos.pheric Chem.istry and Phys.ics, 6(11), 3407-3421, https://doi.org/10.5194/acp-6-3407-2006, 2006.

Walters, W. W., and& Michalski, G.: Theoretical calculation of nitorgen isotope equilibrium exchange fractionation factors for various NO_y molecules, Geochim. Cosmochim. Acta.Geochimica et Cosmochimica Acta, 164, 284-297, http://dx.doi.org/10.1016/j.gca.2015.05.029, 2015.

Walters, W. W., and& Michalski, G.: Theoretical calculation of oxygen equilibrium isotope fractionation factors involving various NO_y molecules, OH, and H_2O and its implications for isotope variations in atmospheric nitrate, Geochim. Cosmochim. Acta.Geochimica et Cosmochimica Acta, 191, 89-101, http://dx.doi.org/10.1016/j.gca.2016.06.039, 2016.

Walters, W. W., Michalski, G., Bohlke, J. K., Alexander, B., Savarino, J., and& Thiemens, M. H.: Assessing the seasonal dynamics of nitrate and sulfate aerosols at the South Pole utilizing stable isotopes, J. Geophys. Res. Atmos.Journal of Geophysical Research: Atmospheres, 124(14), 8161-8177, https://doi.org/10.1029/2019JD030517, 2019.

Walters, W. W., Simonini, D. S., and& Michalski, G.: Nitrogen isotope exchange between NO and NO_2 and its implications for $\delta^{15}N$ variations in tropospheric NO_x and atmospheric nitrate, Geophys. Res. Lett.Geophysical Research Letters, 43, 440-448, https://doi.org/10.1002/2015GL066438, 2016.

Weller, R., Jones, A. E., Wille, A., Jacobi, H.-W., McIntyre, H. P., Sturges, W. T., Huke, M., and& Wagenback, D.: Seasonality of reactive nitrogen oxides (NO_y) at Neumayer Station, Antarctica, J. Geophys. Res. Atmos.Journal of Geophysical Research, 107(D23), 1-11, https://doi.org/10.1029/2002JD002495, 2002.

Williams, J. E., Le Bras, G., Kukui, A., Ziereis, H., and Brenninkmeijer, C. A. M.: The impact of the chemical production of methyl nitrate from the NO + CH_3O_2 reaction on the global distributions of alkyl nitrates, nitrogen oxides and tropospheric ozone: a global modelling study. Atmos.pheric Chem.istry and Phys.ics, 14(5), 2363-2382, https://doi.org/10.5194/acp-14-2363-2014, 2014.

Yeatman, S. G., Spokes, P. F., Dennis, P. F., and& Jickells, T. D.: Coamparisons of aerosol nitrogen isotopic composition at two polluted coastal sites, Atmos.pheric Environ.ments, 35, 1307-1320, https://doi.org/10.1016/S1352-2310(00)00408-8, 2001.

Zong, Z., Wang, X., Tian, C., Chen, Y., Fang, Y., Zhang, F., Li, C., Sun, J., Li, J., and& Zhang, G.: First assessment of NO_x sources at a regional background site in North China using isotopic analysis linked with modeling, Environ. Sci. Technol.Environmental Science and Technology, 51, 5923-5931, https://doi.org/10.1021/acs.est.6b06316, 2017.

Table S1: The starting and ending date, latitude (°S), and longitude(°E) are presented for each aerosol filter deployment. The wind speed (WS; m s^{-1}), atmospheric temperature (Atm T; °C), relative humidity (RH; %), and the number of daylight hours (h) were calculated as an average (Avg) over the duration of each filter deployment. For WS, Atm T and RH the standard deviations (SD) are also shown. Filter deployments are separated into early Summer (ES), Weddell Sea (WS) and late Summer (LS) depending on the location and time of sampling.

Cruise	Collection Dates		Latitude (°S)		Longitude (°E)		WS (m s^{-1})		Atm T (°C)		RH (%)		[1]Sample duration (h)
Leg ID	Start Date	End Date	Start	End	Start	End	Avg	SD	Avg	SD	Avg	SD	
ES 1	2018-12-07	2018-12-08	34.5	37.0	14.8	12.7	5.2	1.8	15.7	0.6	73.4	4.8	24.8
ES 2	2018-12-08	2018-12-09	37.1	41.8	12.6	8.8	5.0	3.3	14.7	1.1	65.9	10.9	13.5
ES 3	2018-12-09	2018-12-10	41.8	44.1	8.8	6.8	9.8	2.3	10.7	0.7	100.3	2.7	14.2
ES 4	2018-12-10	2018-12-12	45.0	50.8	6.1	0.6	13.3	3.1	3.6	1.9	76.6	9.2	15.6
ES 5	2018-12-14	2018-12-16	59.7	68.3	0.0	0.0	6.1	2.0	-2.6	0.6	76.1	8.8	29.5
ES 6	2018-12-16	2018-12-19	68.5	70.1	0.0	-2.1	8.8	4.8	-2.4	1.8	78.3	8.3	27.1
ES 7	2018-12-19	2018-12-21	70.1	70.2	-2.1	-2.1	11.7	1.8	-3.4	1.9	69.5	12.3	39.8
WS 8	2019-01-04	2019-01-06	67.4	64.0	-16.0	-37.0	8.3	4.4	-2.2	0.5	77.4	5.8	42.4
WS 9	2019-01-06	2019-01-08	63.9	62.5	-37.8	-49.2	6.4	3.2	-2.0	0.7	82.9	7.3	34.9
WS 10	2019-01-08	2019-01-10	62.5	65.7	-49.2	-60.2	6.9	3.9	-2.8	0.6	74.3	7.4	28.6
WS 11	2019-01-10	2019-01-12	65.7	66.6	-60.2	-59.6	5.3	1.4	-2.7	1.0	69.2	5.1	25.2
WS 12	2019-01-12	2019-01-14	66.6	66.1	-59.6	-60.4	4.6	1.2	-1.7	0.9	84.0	6.8	37.4
WS 13	2019-01-14	2019-01-16	66.1	65.8	-60.4	-60.5	8.4	2.4	-3.9	1.2	78.7	4.9	26.2
WS 14	2019-01-16	2019-01-18	65.8	65.8	-60.5	-60.7	4.6	0.7	-3.2	1.6	76.4	8.5	22.7
WS 15	2019-01-18	2019-01-20	65.8	66.4	-60.7	-60.3	5.4	1.1	-3.9	0.6	83.8	5.3	32.2
WS 16	2019-01-20	2019-01-22	66.4	66.4	-60.3	-59.9	3.7	1.9	-2.8	0.6	82.5	3.2	33.1
WS 17	2019-01-22	2019-01-26	66.4	64.7	-59.9	-57.2	5.1	2.6	-2.9	0.6	83.4	5.7	37.1
WS 18	2019-01-26	2019-01-28	64.7	63.9	-57.2	-52.0	8.2	1.8	-0.9	0.9	87.4	4.4	29.6
WS 19	2019-01-28	2019-01-31	63.9	62.1	-52.0	-49.9	10.5	4.8	-1.6	0.9	87.8	5.0	35.3
WS 20	2019-01-31	2019-02-01	62.1	62.2	-50.1	-58.9	7.0	3.6	-1.0	2.2	79.8	5.7	39.4
WS 21	2019-02-01	2019-02-06	62.2	61.9	-58.9	-48.7	10.4	3.1	1.5	0.9	89.4	5.0	88.4
WS 22	2019-02-06	2019-02-09	62.0	69.0	-48.2	-52.0	7.7	4.1	-3.6	3.1	87.6	4.1	48.6
WS 23	2019-02-09	2019-02-11	69.0	68.6	-52.0	-52.4	5.6	1.8	-6.2	1.8	80.7	3.3	34.4
WS 24	2019-02-11	2019-02-13	68.6	68.8	-52.4	-51.8	3.3	2.0	-7.8	1.1	82.6	3.8	23.6
WS 25	2019-02-13	2019-02-16	68.8	68.9	-51.8	-41.3	6.9	3.9	-5.2	1.5	81.7	6.5	37.7
WS 26	2019-02-16	2019-02-19	68.9	69.5	-41.3	-8.6	11.9	4.5	-0.6	0.5	90.3	5.5	75.8
WS 27	2019-02-19	2019-02-21	69.6	70.3	-8.2	-2.7	8.2	2.9	-5.3	2.3	76.1	8.1	38.9
LS 28	2019-02-27	2019-03-01	69.3	60.0	-4.0	-2.3	8.6	2.4	-0.7	1.4	74.1	6.5	40.6
LS 29	2019-03-01	2019-03-03	60.0	59.5	-2.8	-26.1	10.1	4.3	-0.2	0.6	80.8	5.3	38.8
LS 30	2019-03-03	2019-03-04	59.5	55.9	-26.1	-33.8	13.0	3.7	0.2	0.9	71.4	5.8	26.2
LS 31	2019-03-04	2019-03-10	55.8	49.5	-34.0	4.1	16.4	7.5	4.2	1.4	88.8	6.6	33.1
LS 32	2019-03-10	2019-03-12	49.5	43.1	4.1	7.8	11.9	2.4	8.6	2.5	90.0	4.7	34.1
LS 33	2019-03-12	2019-03-13	43.1	36.3	7.8	13.3	11.5	1.0	17.5	2.6	84.3	4.0	34.9
LS 34	2019-03-13	2019-03-14	36.1	34.4	13.4	17.8	10.2	2.3	20.0	0.4	82.1	5.0	18.1

[1] The difference in the pump's hour meter reading before and after a filter sample deployment. A sector collector was used to restrict HV-AS activity to avoid contamination from ship stack emissions (Campbell Scientific Africa). The HV-AS only began operating if the wind was blowing at an angle less than 75° or greater than 180° from the bow of the ship for a minimum of ten minutes at a speed of at least 1 m s^{-1}.

Table S2: Accepted reference values for $\delta^{15}N$ vs. N_2 in air and $\delta^{18}O$ vs. VSMOW in ‰ for the calibration standards used. The pooled standard deviation in ‰ and sample size (1 SD_p, n = x) is also reported.

Standard	**IAEA-N3**	**USGS34**	**USGS35**	**Citation**
$\delta^{15}N$	4.7 (0.12, n = 61)	-1.8 (0.09, n = 61)		Böhlke et al., 2003
$\delta^{18}O$	25.6 (0.57, n = 61)	-27.9 (0.54, n = 61)	57.5 (0.44, n = 65)	Böhlke et al., 2003

Table S3: The mass weighted average N and O isotopic composition of atmospheric coarse mode NO_3^- (> 1μm) are shown ($\delta^{15}N$-NO_3^- and $\delta^{18}O$-NO_3^-; ‰), along with total coarse-mode nitrate concentration ([NO_3^-]; ng m^{-3}). The average (Avg) and standard deviation (SD) for the duration of each filter deployment are shown. Filter deployments are separated into early summer (ES), Weddell Sea (WS) and late summer (LS) depending on the location and time of sampling.

Cruise	**[NO_3^-] (ng m^{-3})**		**$\delta^{15}N$-NO_3^- (‰)**		**$\delta^{18}O$-NO_3^- (‰)**	
Leg ID	**Avg**	**SD**	**Avg**	**SD**	**Avg**	**SD**
ES 1	66.6	24.5	-5.0	0.9	36.7	3.7
ES 2	109.4	33.7	-5.7	0.2	40.5	1.7
ES 3	235.0	41.2	-2.7	0.3	51.7	1.8
ES 4	20.0	17.0	-14.5	1.7	16.5	3.2
ES 5	68.6	8.8	-32.2	0.2	70.0	0.5
ES 6	45.3	6.4	-42.9	0.8	62.8	1.4
ES 7	71.7	6.9	-33.5	1.4	52.3	0.6
WS 8	16.2	1.0	-30.9	0.4	53.1	1.0
WS 9	32.9	1.1	-30.1	0.2	53.1	0.4
WS 10	26.8	3.4	-21.0	1.3	48.4	0.6
WS 11	30.2	15.9	-20.1	2.2	23.7	9.5
WS 12	21.5	3.4	-38.1	0.8	60.3	1.9
WS 13	19.8	5.7	-15.9	0.9	23.4	1.4
WS 14	20.5	13.3	-17.1	0.8	20.1	0.7
WS 15	22.0	9.5	-19.6	2.2	28.7	7.2
WS 16	25.7	4.7	-23.9	0.6	30.6	1.9
WS 17	45.4	12.5	-18.2	0.7	29.2	2.7
WS 18	59.5	6.0	-11.6	0.3	42.0	1.4
WS 19	37.7	11.5	-23.5	1.2	18.8	2.0
WS 20	35.0	4.4	-25.0	0.4	51.3	2.1
WS 21	15.1	1.1	-24.2	0.2	52.3	0.6
WS 22	18.3	5.6	-15.5	1.5	45.0	0.7
WS 23	17.7	4.4	-37.8	1.4	50.5	3.8
WS 24	50.6	9.7	-18.7	0.2	28.6	2.0
WS 25	35.3	9.9	-27.7	3.0	34.8	2.0
WS 26	22.7	6.1	-18.4	0.9	43.6	5.8
WS 27	35.8	9.1	-17.0	0.3	30.3	1.8
LS 28	24.5	3.4	-25.6	0.6	50.5	2.8
LS 29	16.9	3.5	-20.8	1.2	51.2	3.7
LS 30	18.8	4.9	-22.4	1.1	43.1	4.24
LS 31	28.7	6.3	-14.0	0.2	44.9	1.6
LS 32	52.2	6.6	-11.2	0.1	45.3	1.4
LS 33	99.3	5.9	-6.6	0.1	57.9	0.8
LS 34	177.4	18.2	-4.6	0.1	58.9	0.9

Table S4: The average (Avg) and standard deviation (SD) sea surface nitrite concentration ([NO_2^-] (μmol L^{-1})) measured during the early summer (ES) and late summer (LS) cruise transects. The date (dd/mm/yyyy), time (GMT), latitude (ºS) and longitude (ºE) of each sample is also given.

Leg	**Date**	**Time**	**Latitude**	**Longitude**	**[NO_2^-] (μmol L^{-1})**	
	(dd/mm/yyyy)	**(GMT)**	**(°S)**	**(°E)**	**Avg**	**SD**
ES	07/12/2018	10:00:00	34.23	17.85	0.13	0.03
ES	07/12/2018	14:00:00	34.50	17.09	0.11	0.01
ES	07/12/2018	18:00:00	34.50	16.17	0.07	0.01
ES	07/12/2018	22:00:00	34.50	15.19	0.09	0.03
ES	08/12/2018	02:00:00	34.77	14.44	0.15	0.00
ES	08/12/2018	06:00:00	35.43	13.93	0.07	0.00
ES	08/12/2018	10:00:00	36.06	13.44	0.13	0.05
ES	08/12/2018	14:00:00	36.64	12.99	0.11	0.04
ES	08/12/2018	18:00:00	37.22	12.54	0.21	0.09
ES	08/12/2018	22:00:00	37.84	12.04	0.16	0.00
ES	09/12/2018	02:00:00	38.57	11.46	0.10	0.02
ES	09/12/2018	06:00:00	39.30	10.88	0.15	0.02
ES	09/12/2018	10:00:00	39.98	10.32	0.21	0.01
ES	09/12/2018	14:00:00	40.70	9.73	0.20	0.02
ES	09/12/2018	18:00:00	41.41	9.14	0.16	0.01
ES	09/12/2018	22:00:00	42.10	8.56	0.14	0.00
ES	10/12/2018	02:00:00	42.82	7.95	0.20	0.02
ES	10/12/2018	06:00:00	43.00	7.79	0.15	0.01
ES	10/12/2018	10:00:00	43.31	7.53	0.30	0.12
ES	10/12/2018	14:00:00	44.00	6.92	0.29	0.03
ES	10/12/2018	18:00:00	44.73	6.29	0.39	0.04
ES	10/12/2018	22:00:00	45.30	5.78	0.37	0.03
ES	11/12/2018	02:00:00	45.80	5.33	0.30	0.00
ES	11/12/2018	06:00:00	46.29	4.90	0.31	0.01
ES	11/12/2018	10:00:00	46.77	4.45	0.33	0.03
ES	11/12/2018	14:00:00	47.32	3.94	0.32	0.02
ES	11/12/2018	18:00:00	47.86	3.44	0.30	0.01
ES	11/12/2018	22:00:00	48.35	2.99	0.31	0.02
ES	12/12/2018	02:00:00	48.82	2.54	0.31	0.02
ES	12/12/2018	06:00:00	49.24	2.14	0.25	0.00
ES	12/12/2018	10:00:00	49.69	1.71	0.31	0.01
ES	12/12/2018	14:00:00	50.09	1.31	0.29	0.05
ES	12/12/2018	18:00:00	50.60	0.82	0.24	0.01
ES	12/12/2018	22:00:00	51.12	0.30	0.33	0.03
ES	13/12/2018	02:00:00	51.73	0.00	0.23	0.04
ES	13/12/2018	06:00:00	52.50	0.00	0.22	0.02
ES	13/12/2018	10:00:00	53.30	0.00	0.24	0.03
ES	13/12/2018	14:00:00	54.00	0.00	0.32	0.01
ES	13/12/2018	18:00:00	54.48	0.00	0.31	0.01
ES	13/12/2018	22:00:00	55.28	-0.06	0.25	0.00
ES	14/12/2018	02:00:00	56.06	0.00	0.21	0.02
ES	14/12/2018	06:00:00	56.89	0.00	0.30	0.01
ES	14/12/2018	10:00:00	57.70	-0.01	0.32	0.02
ES	14/12/2018	14:00:00	58.52	0.00	0.30	0.00
ES	14/12/2018	18:00:00	59.35	-0.01	0.29	0.00
ES	14/12/2018	22:00:00	59.83	-0.01	0.34	0.00

ES	15/12/2018	02:00:00	60.38	-0.05	0.32	0.01
ES	15/12/2018	06:00:00	61.10	0.00	0.28	0.00
ES	15/12/2018	10:00:00	61.58	-0.01	0.29	0.04
ES	15/12/2018	14:00:00	62.30	0.00	0.28	0.02
ES	15/12/2018	18:00:00	62.93	0.00	0.27	0.00
ES	15/12/2018	22:00:00	63.43	-0.02	0.28	0.02
ES	16/12/2018	02:00:00	63.94	0.00	0.25	0.00
ES	16/12/2018	06:00:00	64.50	0.00	0.22	0.02
ES	16/12/2018	10:00:00	65.40	-0.04	0.20	0.01
ES	16/12/2018	14:00:00	66.20	-0.01	0.24	0.01
ES	16/12/2018	18:00:00	66.99	0.00	0.22	0.02
ES	16/12/2018	22:00:00	67.92	-0.05	0.27	0.01
ES	17/12/2018	02:00:00	68.81	0.02	0.27	0.03
LS	27/2/2019	10:00:00	-70.26	-2.72	0.16	0.00
LS	27/2/2019	14:00:00	-69.99	-3.82	0.18	0.01
LS	27/2/2019	18:00:00	-69.64	-3.76	0.17	0.01
LS	27/2/2019	22:00:00	-68.84	-3.76	0.20	0.01
LS	28/2/2019	02:00:00	-67.99	-2.96	0.30	0.01
LS	28/2/2019	06:00:00	-67.04	-2.32	0.20	0.01
LS	28/2/2019	10:00:00	-65.04	-1.44	0.24	0.02
LS	28/2/2019	14:00:00	-64.94	-0.66	0.16	0.02
LS	28/2/2019	18:00:00	-63.90	0.00	0.19	0.00
LS	28/2/2019	22:00:00	-62.82	0.00	0.16	0.02
LS	1/3/2019	02:00:00	-62.18	0.00	0.18	0.00
LS	1/3/2019	06:00:00	-61.27	0.00	0.31	0.01
LS	1/3/2019	10:00:00	-60.16	-0.01	0.39	0.05
LS	1/3/2019	14:00:00	-60.01	-0.86	0.28	0.02
LS	1/3/2019	18:00:00	-59.97	-3.11	0.31	0.01
LS	1/3/2019	22:00:00	-59.88	-5.24	0.26	0.02
LS	2/3/2019	02:00:00	-59.86	-7.35	0.36	0.02
LS	2/3/2019	06:00:00	-59.79	-9.49	0.34	0.02
LS	2/3/2019	10:00:00	-59.73	-11.58	0.34	0.00
LS	2/3/2019	14:00:00	-59.74	-13.69	0.35	0.02
LS	2/3/2019	18:00:00	-59.70	-15.84	0.18	0.02
LS	2/3/2019	22:00:00	-59.64	-17.96	0.39	0.02
LS	3/3/2019	02:00:00	-59.62	-20.08	0.25	0.01
LS	3/3/2019	06:00:00	-59.58	-22.17	0.27	0.01
LS	3/3/2019	10:00:00	-59.54	-24.33	0.29	0.02
LS	3/3/2019	14:00:00	-59.48	-26.34	0.30	0.01
LS	3/3/2019	22:00:00	-59.00	-28.37	0.33	0.02
LS	4/3/2019	02:00:00	-58.32	-29.59	0.40	0.02
LS	4/3/2019	06:00:00	-57.62	-30.83	0.30	0.03
LS	4/3/2019	10:00:00	-56.99	-31.92	0.31	0.02
LS	4/3/2019	14:00:00	-56.48	-32.78	0.28	0.02
LS	4/3/2019	18:00:00	-55.96	-33.65	0.31	0.01
LS	4/3/2019	22:00:00	-55.43	-34.53	0.27	0.03
LS	5/3/2019	02:00:00	-54.89	-35.39	0.24	0.01
LS	5/3/2019	22:00:00	-54.18	-35.46	0.34	0.02
LS	6/3/2019	02:00:00	-54.17	-33.59	0.31	0.02
LS	6/3/2019	06:00:00	-54.16	-31.71	0.37	0.00
LS	6/3/2019	10:00:00	-54.15	-29.83	0.38	0.01

LS	6/3/2019	14:00:00	-54.11	-27.89	0.24	0.01
LS	6/3/2019	18:00:00	-54.12	-26.02	0.28	0.00
LS	6/3/2019	22:00:00	-54.01	-24.19	0.32	0.02
LS	7/3/2019	02:00:00	-54.12	-22.83	0.32	0.04
LS	7/3/2019	06:00:00	-54.12	-21.44	0.23	0.01
LS	7/3/2019	10:00:00	-54.09	-19.56	0.28	0.03
LS	7/3/2019	14:00:00	-54.09	-17.59	0.29	0.01
LS	7/3/2019	18:00:00	-54.09	-15.65	0.30	0.03
LS	7/3/2019	22:00:00	-54.09	-13.72	0.21	0.01
LS	8/3/2019	02:00:00	-54.06	-12.25	0.21	0.04
LS	8/3/2019	06:00:00	-54.06	-10.90	0.29	0.05
LS	8/3/2019	10:00:00	-54.04	-8.79	0.31	0.04
LS	8/3/2019	14:00:00	-54.04	-7.01	0.49	0.02
LS	8/3/2019	18:00:00	-54.03	-5.09	0.27	0.04
LS	8/3/2019	22:00:00	-54.02	-3.46	0.42	0.01
LS	9/3/2019	02:00:00	-54.01	-1.82	0.32	0.01
LS	9/3/2019	06:00:00	-54.00	-0.16	0.35	0.01
LS	9/3/2019	10:00:00	-53.56	-0.02	0.36	0.03
LS	9/3/2019	14:00:00	-52.78	0.00	0.26	0.01
LS	9/3/2019	18:00:00	-52.05	0.00	0.24	0.02
LS	9/3/2019	22:00:00	-51.45	0.00	0.32	0.09
LS	10/3/2019	02:00:00	-51.01	-0.22	0.27	0.03
LS	10/3/2019	06:00:00	-50.68	0.08	0.22	0.01
LS	10/3/2019	10:00:00	-50.40	1.43	0.32	0.08
LS	10/3/2019	14:00:00	-50.15	2.85	0.25	0.02
LS	10/3/2019	18:00:00	-49.61	3.95	0.32	0.03
LS	10/3/2019	22:00:00	-48.95	4.90	0.26	0.01
LS	11/3/2019	02:00:00	-48.23	5.82	0.36	0.09
LS	11/3/2019	06:00:00	-47.56	6.75	0.30	0.01
LS	11/3/2019	10:00:00	-46.76	7.00	0.27	0.01
LS	11/3/2019	14:00:00	-45.87	7.06	0.34	0.04
LS	11/3/2019	18:00:00	-44.99	7.36	0.28	0.01
LS	11/3/2019	22:00:00	-44.13	7.36	0.33	
LS	12/3/2019	00:00:00	-43.79	7.69	0.00	0.05
LS	12/3/2019	04:00:00	-43.18	7.81	0.15	0.04
LS	12/3/2019	08:00:00	-42.89	7.01	0.22	0.00
LS	12/3/2019	12:00:00	-42.12	8.01	0.25	0.11
LS	12/3/2019	16:00:00	-41.34	9.28	0.10	0.00
LS	12/3/2019	20:00:00	-40.54	9.94	0.02	0.01
LS	13/3/2019	00:00:00	-39.72	10.60	0.05	0.07
LS	13/3/2019	04:00:00	-38.89	11.25	0.01	0.01
LS	13/3/2019	08:00:00	-38.06	11.92	0.01	0.01
LS	13/3/2019	12:00:00	-37.24	12.56	0.01	0.01
LS	13/3/2019	16:00:00	-36.42	13.19	0.02	0.01
LS	13/3/2019	20:00:00	-35.58	13.83	0.01	0.01
LS	14/3/2019	00:00:00	-34.92	14.32	0.00	0.00
LS	14/3/2019	04:00:00	-34.50	14.87	0.01	0.01

Table S5: The average (Avg) and standard deviation (SD) for atmospheric nitrate concentration ($[NO_3^-]$ (ng m^{-3})) and nitrogen isotopic composition ($\delta^{15}N\text{-}NO_3^-$) in each aerosol size range: >7 µm, 3 to 7 µm, 1.5 to 3 µm and 1 to 1.5 µm, separated by cruise leg: early summer (ES), Weddell Sea (WS) and late summer (LS).

	$[NO_3^-]$ (ng m^{-3})			**$\delta^{15}N\text{-}NO_3^-$ (‰ vs. N_2)**		
	ES Avg (SD)	**WS Avg (SD)**	**LS Avg (SD)**	**ES Avg (SD)**	**WS Avg (SD)**	**LS Avg (SD)**
>7 µm	10.7 (17.4)	4.1 (4.3)	6.9 (6.0)	-12.2 (11.2)	-14.6 (5.1)	-10.4 (2.7)
3 to 7 µm	29.9 (28.9)	7.7 (4.9)	23.3 (25.7)	-18.8 (14.9)	-25.8 (9.0)	-13.7 (6.0)
1.5 to 3 µm	27.1 (19.3)	9.4 (3.6)	17.9 (17.7)	-20.1 (16.5)	-24.5 (6.6)	-15.9 (8.3)
1 to 1.5 µm	20.5 (6.4)	8.3 (3.4)	11.6 (6.0)	-19.7 (15.5)	-23.0 (7.4)	-16.7 (9.5)

Table S6: Estimated contribution of alkyl nitrates, lightning NO_x, and snow emissions to atmospheric NO_3^- formation for early summer (ES) and late summer (LS) filter deployments. The $\delta^{15}N$ signature of NO_3^- derived from oceanic alkyl nitrates is also presented ($\delta^{15}N\text{-}NO_{3\,AN}^-$) for samples with an alkyl nitrate source > 10%.

Cruise leg ID	**Alkyl nitrates (%)**	**Lightning (%)**	**Snow emissions (%)**	**[1]$\delta^{15}N\text{-}NO_{3\,AN}^-$ (‰)**
ES 1	42.7	57.3	0.0	-11.7
ES 2	29.1	70.8	0.0	-19.7
ES 3	4.5	95.3	0.0	-
ES 4	97.0	3.0	0.0	-14.9
ES 5	81.3	0.0	18.7	-28.6
ES 6	35.1	0.0	64.9	-33.4
ES 7	1.9	0.0	98.1	-
LS 28	95.7	0.0	4.3	-24.7
LS 29	89.9	0.0	10.1	-17.8
LS 30	77.2	0.0	22.8	-14.8
LS 31	86.4	13.6	0.0	-16.2
LS 32	34.0	66.0	0.0	-33.0
LS 33	26.6	73.4	0.0	-24.9
LS 34	8.5	91.5	0.0	-

[1] The '-'symbol indicates samples where alkyl nitrate contributions to total NO_3^- were less than 10%, such that the $\delta^{15}N\text{-}NO_3^-$ signature derived from oceanic alkyl nitrates ($\delta^{15}N\text{-}NO_{3\,AN}^-$) could not be determine with confidence.

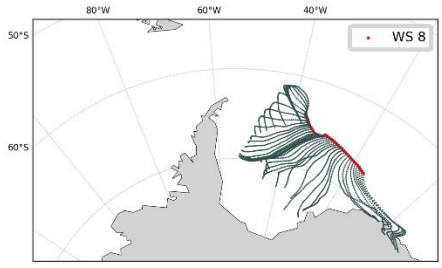
80°W
60°W
40°W
50°S
60°S
WS 8

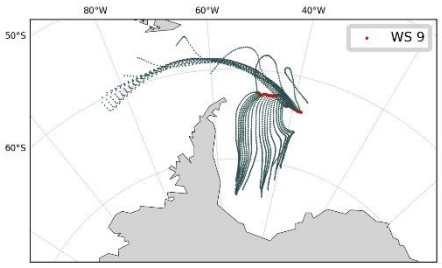
80°W
60°W
40°W
50°S
60°S
WS 9

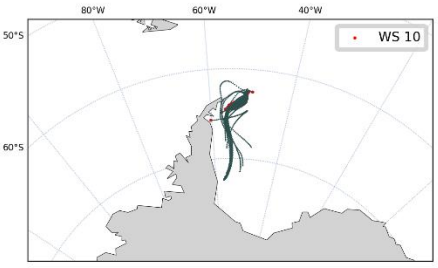
80°W
60°W
40°W
50°S
60°S
WS 10

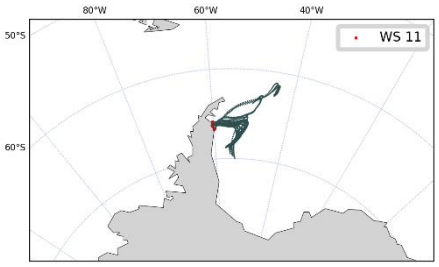
80°W
60°W
40°W
50°S
60°S
WS 11

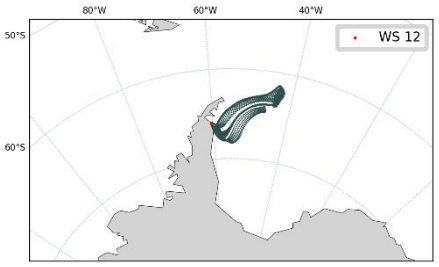
80°W
60°W
40°W
50°S
60°S
WS 12

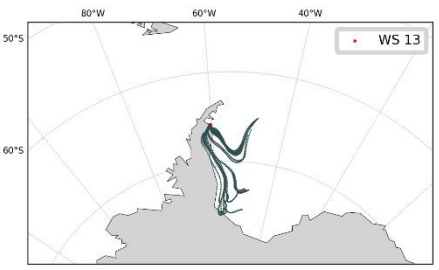
80°W
60°W
40°W
50°S
60°S
WS 13

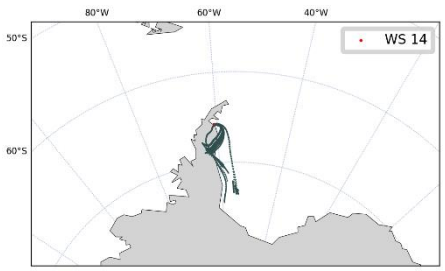
80°W
60°W
40°W
50°S
60°S
WS 14

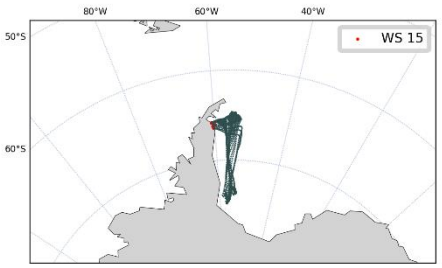
80°W
60°W
40°W
50°S
60°S
WS 15

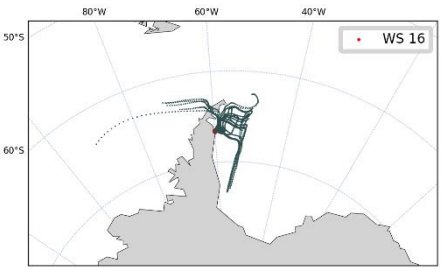
80°W
60°W
40°W
50°S
60°S
WS 16

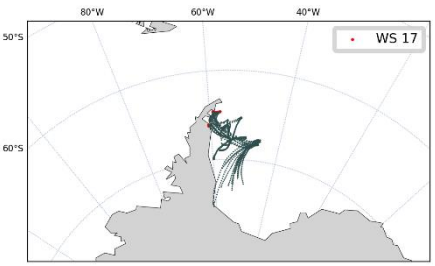
80°W
60°W
40°W
50°S
60°S
WS 17

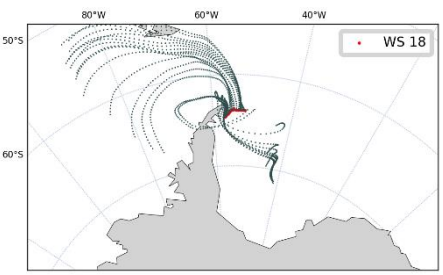
80°W
60°W
40°W
50°S
60°S
WS 18

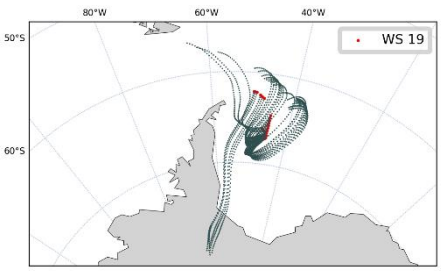
80°W
60°W
40°W
50°S
60°S
WS 19

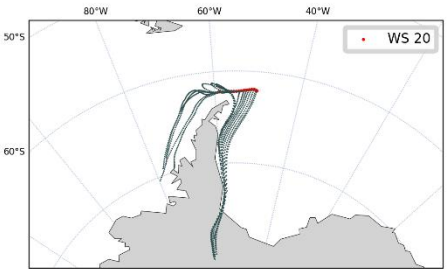
80°W
60°W
40°W
50°S
60°S
WS 20

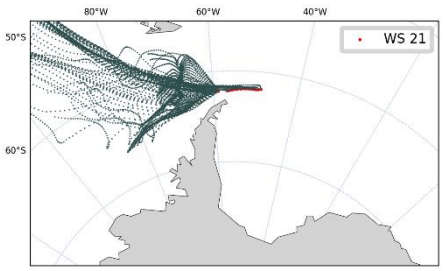
80°W
60°W
40°W
50°S
60°S
WS 21

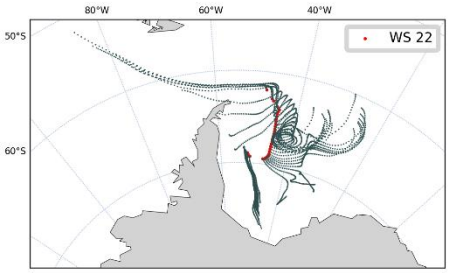
80°W
60°W
40°W
50°S
60°S
WS 22

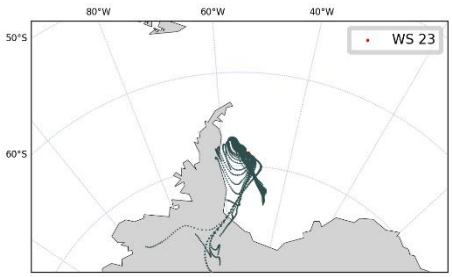
80°W
60°W
40°W
50°S
60°S
WS 23

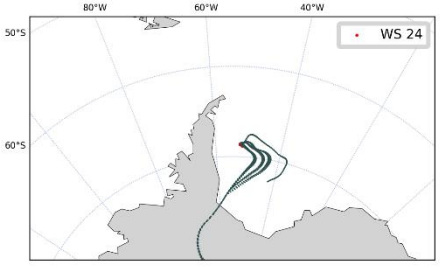
80°W
60°W
40°W
50°S
60°S
WS 24

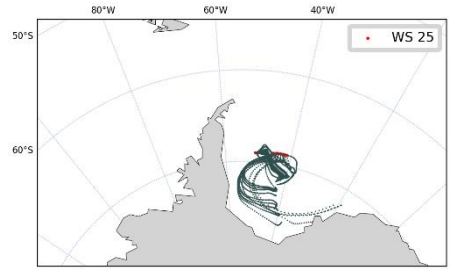
80°W
60°W
40°W
50°S
60°S
WS 25

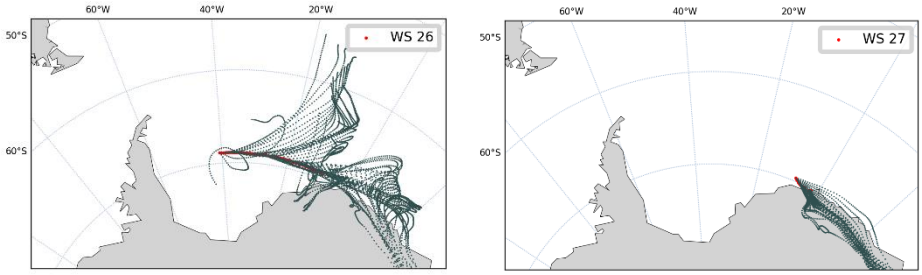

Figure S1. Maps depicting the 72-hour AMBTs computed each hour for all filter deployments (dark grey dots) during the Weddell Sea leg of the research voyage. Each subplot represents one filter deployment, and the cruise leg ID (Tables S1 and S3) is shown in the legend on the upper right-hand side of each subplot. The red dots highlight the ships path.

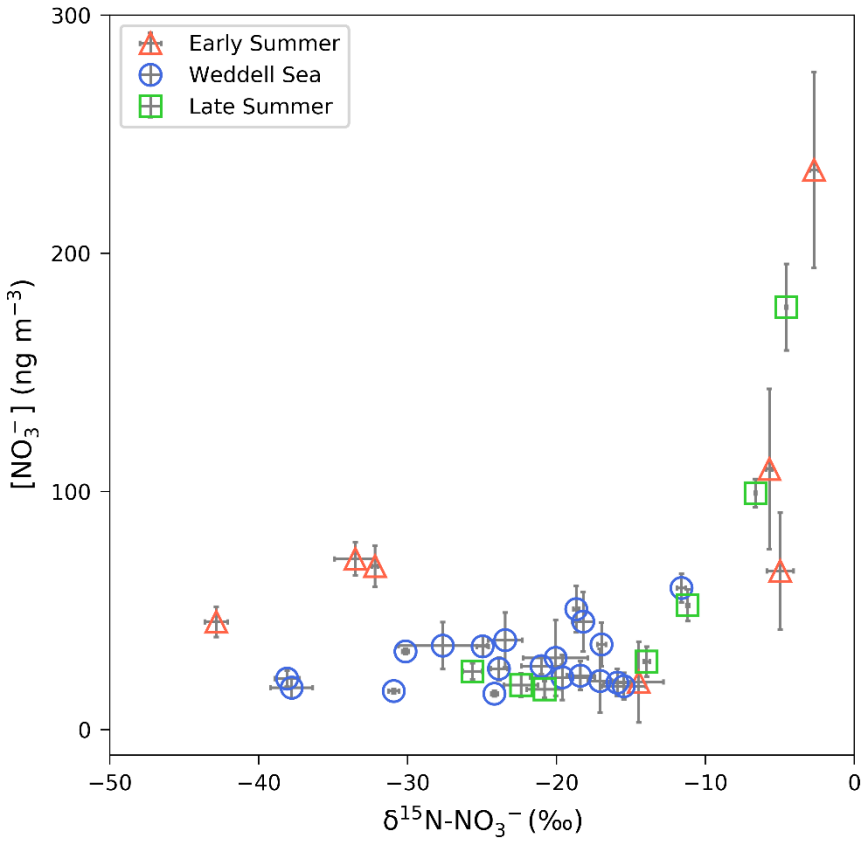

Figure S2. The average (± 1 SD) coarse mode (> 1 µm) nitrate concentration [NO_3^-] (ng m^{-3}), plotted as a function of the weighted average (± 1 SD) $\delta^{15}N\text{-}NO_3^-$ (‰ vs. N_2). Early and late summer latitudinal transects are denoted by the red triangles and green squares, respectively. Weddell Sea samples are denoted by blue circles. Where error bars (± 1 SD) are not visible, the standard deviation is smaller than the size of the marker.